



Image-Based Lunar Terrain Relative Navigation Without a Map: Measurements

John A. Christian,* Lillian Hong,[†] and Paul McKee[‡]

Rensselaer Polytechnic Institute, Troy, New York 12180

Randall Christensen[§]

Utah State University, Logan, Utah 84322

and

Timothy P. Crain[¶]

Intuitive Machines, LLC, Houston, Texas 77058

<https://doi.org/10.2514/1.A34875>

Image-based terrain relative navigation is expected to play an important role in the safe operation of upcoming lunar exploration missions. This work provides a detailed treatment of how visual odometry direction-of-motion measurements may be constructed using images from a monocular camera and without the need of an onboard map of the lunar surface. Substantial care is required to achieve best-possible navigation performance, which numerical studies indicate is sufficient to enable many types of autonomous navigation. Results are shown for historical Apollo images and for synthetic images. While visual odometry alone may not meet every mission's needs, it is a powerful technique that should be a part of every professional spacecraft navigator's toolkit.

I. Introduction

WITH increased interest in exploration of the lunar surface has come a greater need for autonomous navigation. Of particular importance is navigation in low lunar orbit (LLO) and during descent for a lunar landing. In both cases, terrain relative navigation (TRN) is a promising solution—with conventional TRN architectures making use of camera images, light detection and ranging (LIDAR) data, and other measurements [1]. For absolute navigation, specific surface features (i.e., landmarks) are often associated with their corresponding location in a digital elevation map (DEM) of the lunar surface. This approach, however, requires the vehicle carry an onboard map (often taking the form of a catalog of landmarks) and that real-time observations be matched with this onboard map [2–4]. Solving the measurement-to-map correspondence problem is nontrivial and is often the source of large development and testing efforts.

An alternative approach is to perform the mapless tracking of opportunistically-selected features from image to image and use the result to infer the relative motion between the surface and the camera. The practical advantages of using unknown (or unidentified) landmarks and their utility for navigation have been clear since the early days of spaceflight [5–7]. This foundational work from the mid-1960s explored how to navigate a crewed spacecraft using manual sightings of unknown landmarks that were found to be convenient in real time by the astronauts. Since then, manual sightings by astronauts (usually with a scope) have given way to the automatic localization of landmark coordinates in digital images collected by a camera—where convenient landmarks are now found via image processing techniques (e.g., keypoint detection). Meanwhile, the advent (also, coincidentally, in the mid-1960s [8]) and maturation of the field of computer

vision led to a revolution in mathematical tools for multiview geometry [9]. These advances provide modern practitioners of map-free TRN a better framework for interpreting raw image measurements, as exemplified by the Mars Exploration Rover's Decent Image Motion Estimation System (DIMES) [10].

Visual odometry [11–13] is the generic task of using the apparent movement of object points in an image sequence to infer the change in relative position (with an unknown scale) and the change in attitude between a camera and the observed object. The change in position and attitude are collectively referred to as the change in pose. Thus, for the case of TRN, a visual odometry measurement produces the change in pose between the camera and the lunar surface. Solving for change in pose from visual odometry requires no knowledge of the location of the tracked points on the object—only an assurance that those points are rigidly affixed to the observed object. Consequently, TRN using visual odometry requires no a priori knowledge of the observed terrain, though the advantage of not needing a map comes at the expense of introducing a scale ambiguity. If the apparent motion between images is very small, as might happen with a video feed, one may construct an optical flowfield. Popular optical flow algorithms, such as the Lucas–Kanade method [14], compute local velocity vectors (in pixel space) by looking at the spatial and temporal changes in image intensity between two image frames. This is not the framework used here. Instead, the work contained in this paper presumes the two images are separated substantially in time, such that there may be appreciable movement of landmarks between one image and the next. The potentially large motion of features in image space renders the gradient-based approach of optical flow ineffectual for the problem at hand.

The approach presented in this paper uses a feature-based framework. Given an image pair, features are found in each image and correspondence is determined via feature descriptors and/or geometry [15,16]. Change in surface-to-camera pose may be determined (with an unknown scale in translation) without ever needing to solve for the three-dimensional (3-D) location of the observed features using Nistér's five-point algorithm [17]. This classical computer vision result may be considerably simplified for the task of lunar TRN since the change in inertial attitude of both the spacecraft and Moon are well known from other sources (e.g., spacecraft attitude from star tracker and/or gyroscopes, lunar attitude from Spacecraft, Planet, Instrument, Camera-matrix, Events (SPICE) kernels [18,19]). Change in the terrain relative attitude may sometimes be determined from gyroscope measurements alone. In both cases, the result is a visual-inertial framework that is straightforward to develop.

Received 9 June 2020; revision received 15 June 2020; accepted for publication 13 August 2020; published online 30 October 2020. Copyright © 2020 by J. Christian, L. Hong, P. McKee, R. Christensen, and T. Crain. Published by the American Institute of Aeronautics and Astronautics, Inc., with permission. All requests for copying and permission to reprint should be submitted to CCC at www.copyright.com; employ the eISSN 1533-6794 to initiate your request. See also AIAA Rights and Permissions www.aiaa.org/randp.

*Associate Professor, Department of Mechanical, Aerospace, and Nuclear Engineering. Associate Fellow AIAA.

[†]Undergraduate Student, Games and Simulation Arts and Sciences.

[‡]Graduate Research Assistant, Department of Mechanical, Aerospace, and Nuclear Engineering.

[§]Assistant Professor, Department of Electrical and Computer Engineering.

[¶]Vice President of Research and Development. Senior Member AIAA.

Supposing a known change in surface-relative attitude, the pixel locations of corresponding landmarks in an image pair may be used to construct a direction-of-motion measurement. The direction of motion is defined as a unit vector pointing along the change in camera position between the two image times, where only the direction (and not the actual change in position) is observable since scale is ambiguous. The proper construction of this direction-of-motion measurement is the primary topic of this paper.

Though navigation with visual odometry direction-of-motion measurements is the focus of the present work, the authors are not suggesting that a generic lunar exploration spacecraft may be navigated with visual odometry as the only type of TRN measurement. There are certainly situations where explicitly tying image observations to absolute points on the lunar surface or processing range measurements to the lunar surface are required [20,21]. Instead, the authors suggest that visual odometry is a powerful variant of TRN measurement that is appropriate for many phases of flight and should be an element within the professional spacecraft navigator's toolkit.

The visual odometry direction-of-motion measurement developed here (summarized in Sec. IV) may be used without modification to navigate near any celestial body with a visible solid surface and a well-known inertial attitude (e.g., Moon, Mars, an many of the regular moons of Jupiter or Saturn). Navigation near bodies with poorly known attitude (e.g., asteroids) or chaotic attitude (e.g., Hyperion [22]) may be performed by a straightforward application of classical visual odometry techniques. However, classical visual odometry techniques should not be used to navigate when relative attitude is well known, since solving for full relative pose usually reduces performance due to high correlation of errors in the attitude and translational components of these visual odometry measurements.

Finally, this work presents a detailed and step-by-step development of the direction-of-motion measurement for the benefit of the aerospace practitioner who may be unfamiliar with past developments in computer vision. The authors hope the result is an approachable discussion that facilitates the broader adoption of computer vision techniques within the spacecraft guidance, navigation, and control community.

II. Multiview Geometry of the Lunar Surface

Consider a spacecraft equipped with a single monocular camera and an inertial measurement unit (IMU). Now, suppose this spacecraft is moving along a trajectory above the lunar surface and oriented such that the camera captures an image of the terrain below. Further suppose this situation repeats itself over time, such that a sequence of images is collected with considerable terrain overlap between sequential images. In such a scenario, the apparent motion of opportunistically-selected surface features (landmarks) from one image to another provides information on the motion of the camera, and

therefore information on the motion of the spacecraft. Absolute scale is ambiguous when using only opportunistically-selected landmarks within a visual odometry framework; thus, only the direction of motion from the first camera to the second camera location may be found. This direction of motion is expressed as a unit vector that may be provided to a real-time navigation filter.

The geometry of the spacecraft's motion relative to the lunar surface is most straightforwardly described in a Moon-fixed frame, such that the locations of landmarks are described by constant vectors. Since the Moon-fixed frame is rotating with respect to an inertially fixed frame, let the Moon-centered Moon-fixed (MCMF) frame at time t_k be denoted by M_k and the Moon-centered inertial (MCI) frame be denoted I . The MCMF and MCI frames share a common origin (center of the Moon) and only differ by a rotation that may be obtained at any time t_k using SPICE kernels [18,19].

While the multiview geometry is clearer in the MCMF frame, spacecraft dynamics are clearer (and navigation filters are usually written) in the inertial frame. Therefore, it becomes necessary to deal with the MCMF and MCI conventions simultaneously, which is facilitated by Fig. 1. Common angles have been highlighted with a common color to assist with a comparison between the two frame conventions.

Now, consider a pair of two sequential digital images, with the first image at time t_{k-1} and MCI position $\mathbf{r}_{I_{k-1}}$ and the second image at time t_k and MCI position \mathbf{r}_{I_k} . As shown in Fig. 1, define the change in MCMF position between the two image times by the vector \mathbf{s}_{M_k} , such that

$$\mathbf{s}_{M_k} = \mathbf{T}_{M_k}^I \mathbf{r}_{I_k} - \mathbf{T}_{M_{k-1}}^I \mathbf{r}_{I_{k-1}} \quad (1)$$

where $\mathbf{T}_{M_k}^I$ is the attitude transformation matrix (passive interpretation of a rotation [23]) that transforms a vector expressed in frame I to the same vector expressed in frame M_k .

The inertial orientation of the spacecraft—and, therefore, the orientation of the camera—may change between the first image time and the second image time. The inertial orientation of the Moon also changes during this time. Denote the camera frame at t_k as C_k , such that one may express the vector \mathbf{s} in frame C_k :

$$\mathbf{s}_{(C_k)_k} = \mathbf{T}_{C_k}^{M_k} \mathbf{s}_{M_k} = \mathbf{T}_{C_k}^{M_k} (\mathbf{r}_{M_k} - \mathbf{r}_{M_{k-1}}) \quad (2)$$

where $\mathbf{T}_{C_k}^{M_k}$ is the attitude transformation matrix that transforms a vector expressed in frame M_k to the same vector expressed in frame C_k . It is advantageous to express \mathbf{s} in the camera frame at time t_k since this procedure is ultimately intended to produce a measurement for use in a sequential filter.

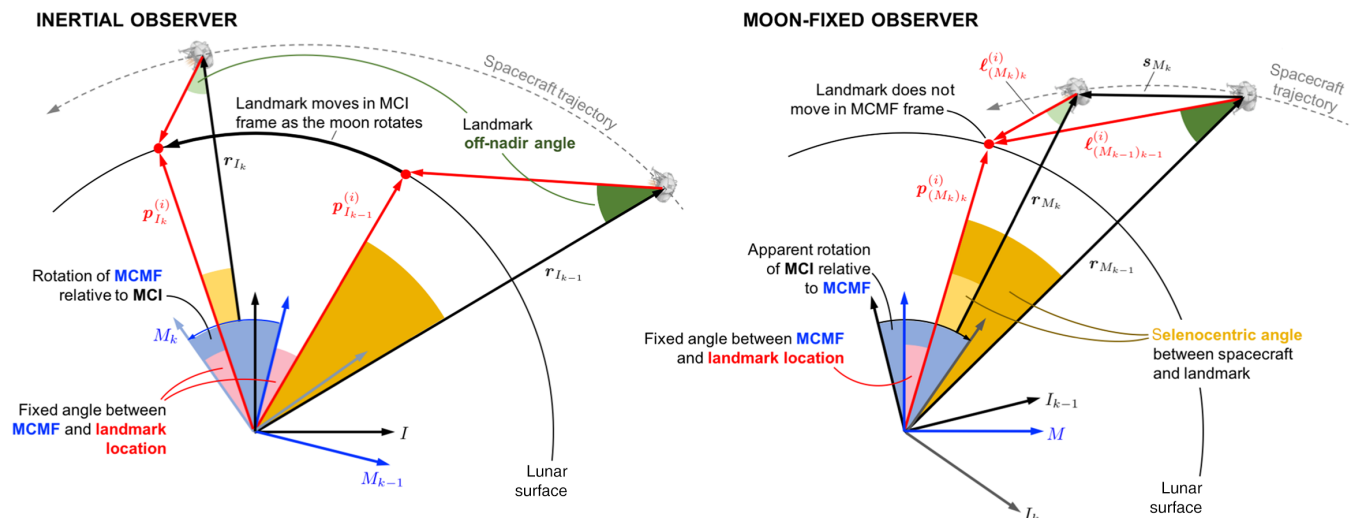


Fig. 1 Geometry for two sightings of the same landmark as illustrated in the MCI frame (left) and MCMF frame (right).

Now suppose that the spacecraft observes the same landmark in both images. If the MCMF location of the i th landmark is $\mathbf{p}_M^{(i)}$, then simple geometry shows that

$$\ell_{(M_k)_k}^{(i)} = \mathbf{p}_{M_k}^{(i)} - \mathbf{T}_{M_k}^I \mathbf{r}_{I_k} \quad (3)$$

where $\ell_{(M_k)_k}^{(i)}$ is the vector from the spacecraft to the i th landmark at time t_k in the MCMF frame. The MCMF difference in the relative position of the camera and landmark is

$$\ell_{(M_{k-1})_{k-1}}^{(i)} - \ell_{(M_k)_k}^{(i)} = (\mathbf{p}_{M_{k-1}}^{(i)} - \mathbf{T}_{M_{k-1}}^I \mathbf{r}_{I_{k-1}}) - (\mathbf{p}_{M_k}^{(i)} - \mathbf{T}_{M_k}^I \mathbf{r}_{I_k}) \quad (4)$$

Then, recalling Eq. (1) and that the landmarks are fixed in the MCMF frame,

$$\mathbf{p}_M^{(i)} = \mathbf{p}_{M_k}^{(i)} = \mathbf{p}_{M_{k-1}}^{(i)} \quad (5)$$

it is easy to show that Eq. (4) becomes (see simplified schematic in Fig. 2)

$$\ell_{(M_{k-1})_{k-1}}^{(i)} - \ell_{(M_k)_k}^{(i)} = \mathbf{s}_{M_k} \quad (6)$$

and, therefore, that

$$\ell_{(M_k)_k}^{(i)} = \ell_{(M_{k-1})_{k-1}}^{(i)} - \mathbf{s}_{M_k} \quad (7)$$

where, conveniently, \mathbf{p} vanishes and knowledge of the landmark's actual location is not necessary.

Cameras fundamentally produce line-of-sight (LOS) measurements. Optical observations of the i th landmark at time t_k will produce a LOS unit vector in the direction of $\ell_k^{(i)}$ as expressed in frame C_k . Therefore, it becomes convenient to start bookkeeping the landmark vectors in their native frames. Rewriting Eq. (7) with the relative landmark vectors in the appropriate camera frame yields

$$\mathbf{T}_{M_k}^{C_k} \ell_{(C_k)_k}^{(i)} = \mathbf{T}_{M_{k-1}}^{C_{k-1}} \ell_{(C_{k-1})_{k-1}}^{(i)} - \mathbf{s}_{M_k} \quad (8)$$

This MCMF geometry may be expressed in frame C_k by left multiplying by $\mathbf{T}_{C_k}^{M_k}$

$$\ell_{(C_k)_k}^{(i)} = \mathbf{T}_{C_k}^{M_k} \mathbf{T}_{M_{k-1}}^{C_{k-1}} \ell_{(C_{k-1})_{k-1}}^{(i)} - \mathbf{s}_{(C_k)_k} \quad (9)$$

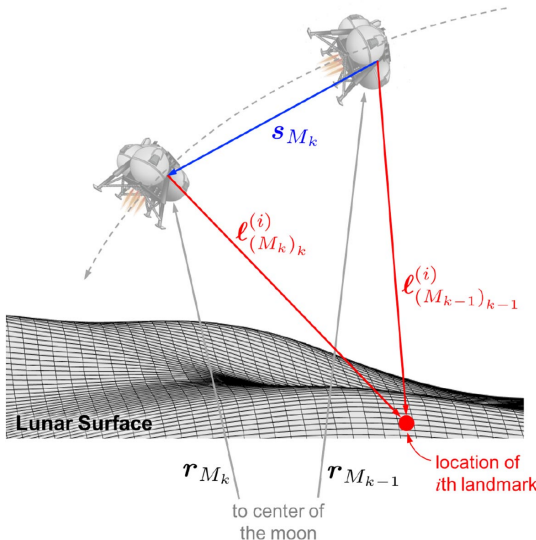


Fig. 2 Simplified MCMF geometry of a spacecraft viewing a common landmark on the lunar surface from two points along its trajectory.

where the term $\mathbf{T}_{C_k}^{M_k} \mathbf{T}_{M_{k-1}}^{C_{k-1}}$ describes the change in camera attitude between t_{k-1} and t_k relative to the inertially rotating MCMF frame. To compact notation, let the camera's MCMF-relative attitude change be defined as

$$\mathbf{M}_{C_k}^{C_{k-1}} = \mathbf{T}_{C_k}^{M_k} \mathbf{T}_{M_{k-1}}^{C_{k-1}} \quad (10)$$

such that Eq. (9) may be rewritten as

$$\ell_{(C_k)_k}^{(i)} = \mathbf{M}_{C_k}^{C_{k-1}} \ell_{(C_{k-1})_{k-1}}^{(i)} - \mathbf{s}_{(C_k)_k} \quad (11)$$

Inspection of the geometry reveals that the vectors $\ell_{k-1}^{(i)}$, $\ell_k^{(i)}$, and \mathbf{s}_k are all coplanar in the MCMF frame (see Fig. 2) since they form a triangle. Therefore, taking the cross product of both sides of Eq. (11) with $\mathbf{s}_{(C_k)_k}$ produces a vector perpendicular to the triangle formed by the two camera centers and the observed landmark:

$$[\mathbf{s}_{(C_k)_k} \times] \ell_{(C_k)_k}^{(i)} = [\mathbf{s}_{(C_k)_k} \times] \mathbf{M}_{C_k}^{C_{k-1}} \ell_{(C_{k-1})_{k-1}}^{(i)} \quad (12)$$

where $[\cdot \times]$ is the skew-symmetric cross-product matrix defined as $\mathbf{a} \times \mathbf{b} = [\mathbf{a} \times] \mathbf{b}$. Next, left multiply Eq. (12) by $(\ell_{(C_k)_k}^{(i)})^T$, which produces zero since $\ell_{(C_k)_k}^{(i)}$ is in the plane of the triangle:

$$(\ell_{(C_k)_k}^{(i)})^T [\mathbf{s}_{(C_k)_k} \times] \mathbf{M}_{C_k}^{C_{k-1}} \ell_{(C_{k-1})_{k-1}}^{(i)} = 0 \quad (13)$$

which may be written equivalently as

$$(\ell_{(C_{k-1})_{k-1}}^{(i)})^T \mathbf{M}_{C_{k-1}}^{C_k} [\mathbf{s}_{(C_k)_k} \times] \ell_{(C_k)_k}^{(i)} = 0 \quad (14)$$

This produces the so-called *epipolar constraint* found in most textbooks on computer vision [24,25], though the solution is often written with s in the C_{k-1} frame (instead of the C_k frame):

$$(\ell_{(C_{k-1})_{k-1}}^{(i)})^T [\mathbf{s}_{(C_{k-1})_k} \times] \mathbf{M}_{C_{k-1}}^{C_k} \ell_{(C_k)_k}^{(i)} = 0 \quad (15)$$

Regardless of the frame, this constraint may be rewritten in the classical form as

$$(\ell_{(C_{k-1})_{k-1}}^{(i)})^T \mathbf{E} \ell_{(C_k)_k}^{(i)} = 0 \quad (16)$$

where the matrix \mathbf{E} is usually called the *essential matrix*:

$$\mathbf{E} = \mathbf{M}_{C_{k-1}}^{C_k} [\mathbf{s}_{(C_k)_k} \times] = [\mathbf{s}_{(C_{k-1})_k} \times] \mathbf{M}_{C_{k-1}}^{C_k} \quad (17)$$

III. Sensor Models

To make practical use of the epipolar constraint from Eqs. (14) and (16), it is necessary to understand how a camera produces information related to $\ell_{(C_k)_k}^{(i)}$ and how an IMU produces information related to $\mathbf{M}_{C_{k-1}}^{C_k}$. These two relations are developed in the two subsections that follow.

A. Camera Model

This work presumes the navigation camera is well calibrated and that common distortions may be removed. Such calibration schemes are well understood and are discussed extensively elsewhere [26–28]. Therefore, proceeding under the assumption that distortions have been removed, the relationship between an object's actual 3-D location and its apparent location on the image plane may be described by the pinhole camera model.

The camera frame convention used here is the same as Ref. [28], which places the $+z$ -axis direction out of the camera and along the boresight direction. All image analysis is performed in the image plane (instead of the focal plane) for simplicity [28,29], as is shown in Fig. 3. When looking out of the camera, the x axis is to the right

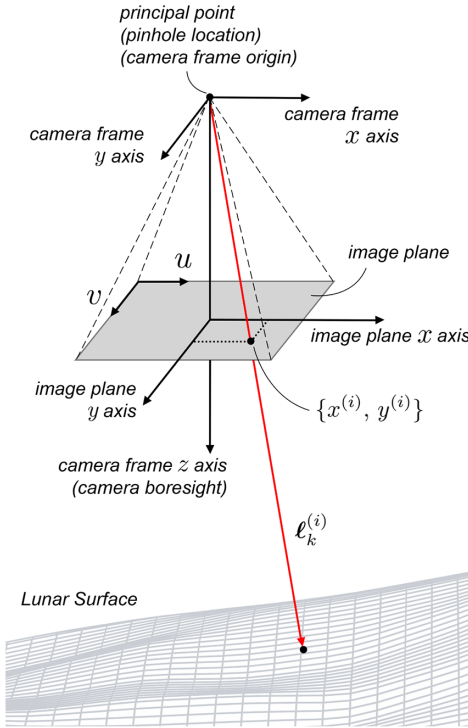


Fig. 3 Graphical depiction of camera frame and image plane.

(direction of increasing column count in image) and the y axis is down (direction of increasing row count in image). The elements of the landmark observation vector ℓ may be written in the camera frame as

$$\ell_{(C_k)_k}^{(i)} = \begin{bmatrix} \ell_{x_k}^{(i)} \\ \ell_{y_k}^{(i)} \\ \ell_{z_k}^{(i)} \end{bmatrix} \quad (18)$$

The pinhole camera model (perfect perspective projection) relates the two-dimensional (2-D) image plane coordinates to these 3-D locations as

$$\bar{x}_k^{(i)} = \frac{\ell_{(C_k)_k}^{(i)}}{\ell_{z_k}^{(i)}} = \begin{bmatrix} x_k^{(i)} \\ y_k^{(i)} \\ 1 \end{bmatrix} \quad (19)$$

Now, recall that pixel coordinates $\{u^{(i)}, v^{(i)}\}$ in an image may be related to image plane coordinates $\{x^{(i)}, y^{(i)}\}$ according to

$$\bar{u}_k^{(i)} = \begin{bmatrix} u_k^{(i)} \\ v_k^{(i)} \\ 1 \end{bmatrix} = \begin{bmatrix} d_x & \alpha & u_p \\ 0 & d_y & v_p \\ 0 & 0 & 1 \end{bmatrix} \begin{bmatrix} x_k^{(i)} \\ y_k^{(i)} \\ 1 \end{bmatrix} \quad (20)$$

where $\{u_p, v_p\}$ is the pixel coordinate of the principal point (where the optical axis pierces the image) and α is the detector skewness. The u - v coordinate system has its origin in the upper left-hand corner of the image, such that integer values of u describe the pixel column number and integer values of v describe the pixel row number. The values of d_x and d_y represent a unit conversion to pixel space and are given by

$$d_x = f/\mu_x \quad d_y = f/\mu_y \quad (21)$$

where f is the focal length and μ is the pixel pitch. More details regarding this camera convention and notation may be found in Refs. [28,29].

In the case where the camera calibration matrix C is known,

$$C = \begin{bmatrix} d_x & \alpha & u_p \\ 0 & d_y & v_p \\ 0 & 0 & 1 \end{bmatrix} \quad (22)$$

it is possible to analytically compute its inverse [29]

$$C^{-1} = \begin{bmatrix} \frac{1}{d_x} & -\frac{\alpha}{d_x d_y} & \frac{\alpha v_p - d_x u_p}{d_x d_y} \\ 0 & \frac{1}{d_y} & -\frac{v_p}{d_y} \\ 0 & 0 & 1 \end{bmatrix} \quad (23)$$

which permits the relations

$$\bar{u}_k^{(i)} = C \bar{x}_k^{(i)} \quad \bar{x}_k^{(i)} = C^{-1} \bar{u}_k^{(i)} \quad (24)$$

Applying this to the measurements at t_{k-1} and t_k ,

$$\ell_{(C_{k-1})_{k-1}}^{(i)} = \ell_{z_{k-1}}^{(i)} \bar{x}_{k-1}^{(i)} = \ell_{z_{k-1}}^{(i)} C^{-1} \bar{u}_{k-1}^{(i)} \quad (25)$$

$$\ell_{(C_k)_k}^{(i)} = \ell_{z_k}^{(i)} \bar{x}_k^{(i)} = \ell_{z_k}^{(i)} C^{-1} \bar{u}_k^{(i)} \quad (26)$$

where, recalling Eq. (20), $\bar{u}_k^{(i)}$ is simply the homogeneous pixel coordinate of the observed landmark in the image collected at time t_k :

$$\bar{u}_k^{(i)} = \begin{bmatrix} u_k^{(i)} \\ v_k^{(i)} \\ 1 \end{bmatrix} \quad (27)$$

B. Inertial Measurement Unit Model

Data from the inertial measurement unit's gyroscopes (gyro) will be used to determine the change in attitude between the two image times. Importantly, the IMU measures the change in inertial attitude $T_{C_k}^{C_{k-1}}$, whereas the direction-of-motion measurement from Eq. (14) requires change in MCMF attitude $M_{C_k}^{C_{k-1}}$.

Begin by assuming a simple strapdown IMU with gyroscopes that produce measurements of the inertial angular velocity in the IMU frame,

$$\tilde{\omega} = \omega + b_g + \nu_g \quad (28)$$

where ω is the angular velocity, b_g is the gyro bias, and ν_g is zero mean white noise. The model of Eq. (28) is the so-called Farrenkopf gyro model [30], which has been used extensively for analysis of navigation systems [31–33]. Consequently, the current estimate of the IMU calibration parameter b_g may be used to compute an estimated angular velocity $\hat{\omega}$:

$$\hat{\omega} = \tilde{\omega} - b_g \quad (29)$$

which may be used to propagate the attitude according to

$$\dot{\hat{q}} = \frac{1}{2} \begin{bmatrix} 0 \\ \hat{\omega} \end{bmatrix} \otimes \hat{q} \quad (30)$$

where \bar{q} is the attitude quaternion and \otimes is the non-Hamiltonian quaternion multiplication operator (sometimes called Shuster's convention [23]). Propagation of Eq. (30) from t_{k-1} to t_k produces the quaternion describing the change in inertial IMU attitude $\bar{q}_{IMU_k}^{IMU_{k-1}}$, which may be converted to its corresponding attitude transformation matrix $T_{IMU_k}^{IMU_{k-1}}$.

The camera frame is generally different from the IMU frame. Therefore, let relative alignment between the IMU and the TRN camera be given by $\mathbf{T}_C^{\text{IMU}}$. For the purposes of the present analysis, this relative alignment is assumed fixed—though a true flight system may wish to estimate updates to this alignment as a state in the navigation filter.

The inertial attitude of the TRN camera at time t_k is given by

$$\mathbf{T}_{C_k}^I = \mathbf{T}_C^{\text{IMU}} \mathbf{T}_{\text{IMU}_k}^I \quad (31)$$

such that the transformation from the MCMF frame to the camera frame is

$$\mathbf{T}_{C_k}^{M_k} = \mathbf{T}_{C_k}^I \mathbf{T}_I^{M_k} = \mathbf{T}_C^{\text{IMU}} \mathbf{T}_{\text{IMU}_k}^I \mathbf{T}_I^{M_k} \quad (32)$$

Recall that when the gyro measurements are integrated from t_{k-1} to t_k , one obtains the change in inertial IMU attitude $\mathbf{T}_{\text{IMU}_k}^{\text{IMU}_{k-1}}$ such that

$$\mathbf{T}_{\text{IMU}_k}^I = \mathbf{T}_{\text{IMU}_k}^{\text{IMU}_{k-1}} \mathbf{T}_{\text{IMU}_{k-1}}^I \quad (33)$$

Consequently, to obtain the value of $\mathbf{M}_{C_k}^{C_{k-1}}$ described in Eq. (10) from the integrated gyro measurements, one must compute

$$\begin{aligned} \mathbf{M}_{C_k}^{C_{k-1}} &= \mathbf{T}_{C_k}^{M_k} \mathbf{T}_{M_{k-1}}^{C_{k-1}} \\ &= \left(\mathbf{T}_C^{\text{IMU}} \mathbf{T}_{\text{IMU}_k}^{\text{IMU}_{k-1}} \mathbf{T}_{\text{IMU}_{k-1}}^I \mathbf{T}_I^{M_k} \right) \left(\mathbf{T}_{M_{k-1}}^I \mathbf{T}_I^{\text{IMU}_{k-1}} \mathbf{T}_{\text{IMU}}^C \right) \end{aligned} \quad (34)$$

Therefore, to compute $\mathbf{M}_{C_k}^{C_{k-1}}$ in the most general case requires knowledge of the IMU's inertial attitude $\mathbf{T}_{\text{IMU}_k}^I$ and of the Moon's inertial attitude $\mathbf{T}_{M_k}^I$ at each image time.

Note that the matrix product $\mathbf{T}_I^{M_k} \mathbf{T}_{M_{k-1}}^I$ in the middle of Eq. (34) describes the apparent change in I seen by an observer in the MCMF frame. Fortunately, the Moon rotates very slowly (about 0.00015 deg/s = 0.55 arcsec/s), such that this change is very small for a pair of sequential images separated by a short time interval. Therefore, for many visual odometry TRN applications, it may be assumed that $\mathbf{T}_I^{M_k} \mathbf{T}_{M_{k-1}}^I \approx \mathbf{I}_{3 \times 3}$, such that Eq. (34) collapses down to

$$\mathbf{M}_{C_k}^{C_{k-1}} \approx \mathbf{T}_C^{\text{IMU}} \mathbf{T}_{\text{IMU}_k}^{\text{IMU}_{k-1}} \mathbf{T}_{\text{IMU}}^C \quad (35)$$

Consequently, $\mathbf{M}_{C_k}^{C_{k-1}}$ may be reasonably computed using just the change in IMU inertial attitude and knowledge of the relative alignment between the IMU and the TRN camera.

IV. Visual Odometry Direction-of-Motion Measurement

Supposing that both IMU measurements and a pair of images with overlapping terrain are available, it is possible to use the pixel coordinates of common landmarks in each image to estimate the direction of motion. The reader is reminded that this may be done with no knowledge of the landmark's actual location on the lunar surface—thus, construction of the visual odometry direction-of-motion measurement is possible without having a map of the Moon.

The results of the camera model may be substituted into the epipolar constraint equation to directly compute the direction of motion from corresponding landmark pixel coordinates. Therefore, substituting Eq. (25) and Eq. (26) into Eq. (16),

$$\left(\ell_{z_{k-1}}^{(i)} \mathbf{C}^{-1} \bar{\mathbf{u}}_{k-1}^{(i)} \right)^T \mathbf{E} \left(\ell_{z_k}^{(i)} \mathbf{C}^{-1} \bar{\mathbf{u}}_k^{(i)} \right) = 0 \quad (36)$$

which simplifies to

$$\left(\bar{\mathbf{u}}_{k-1}^{(i)} \right)^T \mathbf{C}^{-T} \mathbf{E} \mathbf{C}^{-1} \bar{\mathbf{u}}_k^{(i)} = 0 \quad (37)$$

The matrix $\mathbf{F} = \mathbf{C}^{-T} \mathbf{E} \mathbf{C}^{-1}$ is sometimes called the *fundamental matrix*, which produces the usual form of the epipolar constraint in terms of pixel coordinates

$$\left(\bar{\mathbf{u}}_{k-1}^{(i)} \right)^T \mathbf{F} \bar{\mathbf{u}}_k^{(i)} = 0 \quad (38)$$

This equation is linear in \mathbf{F} , and the measurement pairs $\{\tilde{\mathbf{u}}_{k-1}^{(i)}, \tilde{\mathbf{u}}_k^{(i)}\}_{i=1}^n$ may be used to estimate the eight independent parameters in \mathbf{F} (i.e., estimate \mathbf{F} with an arbitrary scaling). Estimation of \mathbf{F} in this way is a standard practice in computer vision, and a great deal has been written on the topic [9]. The problem solved in this work is somewhat simpler, since the both the camera calibration matrix \mathbf{C} and the change in attitude $\mathbf{M}_{C_{k-1}}^{C_k}$ are well known; thus, only the two degrees of freedom describing the direction of motion in frame C_k are unknown.

A. Direct Least-Squares Estimation of the Direction of Motion

To find the least-squares estimate of the direction of motion from the epipolar constraint, substitute \mathbf{E} from Eq. (17) into Eq. (37),

$$\left(\bar{\mathbf{u}}_{k-1}^{(i)} \right)^T \mathbf{C}^{-T} \mathbf{M}_{C_{k-1}}^{C_k} [\mathbf{s}_{(C_k)_k} \times] \mathbf{C}^{-1} \bar{\mathbf{u}}_k^{(i)} = 0 \quad (39)$$

which represents a constraint on the change in pose and the apparent pixel coordinates of a particular landmark in both images. This equation is linear in the unknown $\mathbf{s}_{(C_k)_k}$. To solve for this unknown, rearrange Eq. (39) to into a linear system in the unknown translation $\mathbf{s}_{(C_k)_k}$,

$$\left(\bar{\mathbf{u}}_{k-1}^{(i)} \right)^T \mathbf{C}^{-T} \mathbf{M}_{C_{k-1}}^{C_k} [\mathbf{C}^{-1} \bar{\mathbf{u}}_k^{(i)} \times] \mathbf{s}_{(C_k)_k} = 0 \quad (40)$$

Then, presuming that many points are simultaneously observed, one may write the following linear system:

$$\mathbf{H} \mathbf{s}_{(C_k)_k} = \mathbf{0}_{n \times 1} \quad (41)$$

where

$$\mathbf{H} = \begin{bmatrix} (\bar{\mathbf{u}}_{k-1}^{(1)})^T \mathbf{C}^{-T} \mathbf{M}_{C_{k-1}}^{C_k} [\mathbf{C}^{-1} \bar{\mathbf{u}}_k^{(1)} \times] \\ (\bar{\mathbf{u}}_{k-1}^{(2)})^T \mathbf{C}^{-T} \mathbf{M}_{C_{k-1}}^{C_k} [\mathbf{C}^{-1} \bar{\mathbf{u}}_k^{(2)} \times] \\ \vdots \\ (\bar{\mathbf{u}}_{k-1}^{(n)})^T \mathbf{C}^{-T} \mathbf{M}_{C_{k-1}}^{C_k} [\mathbf{C}^{-1} \bar{\mathbf{u}}_k^{(n)} \times] \end{bmatrix} \quad (42)$$

This result is analogous to the classic eight-point algorithm for estimating the fundamental matrix from point correspondences [9,34], though Eq. (41) uses an $n \times 3$ matrix to solve for $\mathbf{s}_{(C_k)_k}$ and the eight-point algorithm is an $n \times 9$ matrix to solve for the vectorized elements of \mathbf{F} . Clearly, it is only possible to solve for the direction of $\mathbf{s}_{(C_k)_k}$, since the scale of $\mathbf{s}_{(C_k)_k}$ is arbitrary in Eq. (41). The fact that scale is unobservable should come as no surprise, as this is always the case when estimating the fundamental matrix from corresponding point pairs. Recovery of scale requires additional information (e.g., constraining opportunistic landmarks to lie on a reference ellipsoid [35], the absolute map locations of observed landmarks). Therefore, without loss of generality, define \mathbf{s}' to be the unit vector in the direction of \mathbf{s} such that

$$\mathbf{s}'_{(C_k)_k} = \frac{\mathbf{s}_{(C_k)_k}}{\|\mathbf{s}_{(C_k)_k}\|} \quad (43)$$

and the corresponding nondimensionalized fundamental matrix is given by

$$\mathbf{F}' = \mathbf{C}^{-T} \mathbf{E}' \mathbf{C}^{-1} = \mathbf{C}^{-T} \mathbf{M}_{C_{k-1}}^{C_k} [\mathbf{s}'_{(C_k)_k} \times] \mathbf{C}^{-1} \quad (44)$$

Likewise, the linear system from Eq. (41) is rewritten as

$$\mathbf{H}\mathbf{s}'_{(C_k)_k} = \mathbf{0}_{n \times 1} \quad (45)$$

where \mathbf{H} is still from Eq. (42).

Observe that all the quantities in \mathbf{H} are either known (\mathbf{C} and $\mathbf{M}_{C_{k-1}}^{C_k}$) or measured ($\bar{\mathbf{u}}_{k-1}^{(i)}$ and $\bar{\mathbf{u}}_k^{(i)}$). Using the noisy measurements to construct the noisy matrix $\tilde{\mathbf{H}}$, one obtains

$$\tilde{\mathbf{H}}\mathbf{s}'_{(C_k)_k} = \boldsymbol{\epsilon}_{n \times 1} \quad (46)$$

where $\boldsymbol{\epsilon}_{n \times 1}$ is a vector of small residuals. The residuals ϵ_i are usually called the *algebraic distance* for each landmark measurement pair.

Clearly, the true solution for $\mathbf{s}'_{(C_k)_k}$ lies in the one-dimensional null space of \mathbf{H} . Since only the noisy matrix $\tilde{\mathbf{H}}$ is available (which is generally full rank, with a high condition number), one seeks the vector as close as possible to a null space. The least-squares solution to such a problem may be found through a singular value decomposition (SVD). Therefore, taking the SVD of $\tilde{\mathbf{H}}$,

$$\tilde{\mathbf{H}} = \mathbf{U}\mathbf{D}\mathbf{V}^T \quad (47)$$

the solution is the column of \mathbf{V} corresponding to the smallest singular value in \mathbf{D} . Assuming the singular values are sorted largest to smallest, this is the last column of $\mathbf{V} = [\mathbf{v}_1 \ \mathbf{v}_2 \ \mathbf{v}_3]$. The correct sign of \mathbf{v}_3 is found by choosing the sign that puts the observed points in front of both cameras (this will only be the case for one of the sign conventions; see Appendix A).

If measured pixel coordinates $\{\tilde{\bar{\mathbf{u}}}_{k-1}^{(i)}, \tilde{\bar{\mathbf{u}}}_k^{(i)}\}_{i=1}^n$ are used in place of the true pixel coordinates $\{\bar{\mathbf{u}}_{k-1}^{(i)}, \bar{\mathbf{u}}_k^{(i)}\}_{i=1}^n$ to form \mathbf{H} , then the least-squares problem in Eq. (46) produces a biased estimate of $\mathbf{s}'_{(C_k)_k}$. Furthermore, if one were to naively solve the weighted least-squares problem

$$\min J(\mathbf{s}'_{(C_k)_k}) = \boldsymbol{\epsilon}_{n \times 1}^T \mathbf{R}_e^{-1} \boldsymbol{\epsilon}_{n \times 1} = (\mathbf{s}'_{(C_k)_k})^T \tilde{\mathbf{H}}^T \mathbf{R}_e^{-1} \tilde{\mathbf{H}} \mathbf{s}'_{(C_k)_k} \quad (48)$$

the result would still be biased. The existence of such biases is well documented for problems of this form [36–38]. The bias here arises from how the least-squares problem is formed and how the epipolar constraint is applied. Hence, the problem of a biased estimate does not arise from the weights of the least-squares solution but in the choice of the distance metric to be minimized (i.e., the choice to minimize the algebraic distances in $\boldsymbol{\epsilon}_{n \times 1}$).

The authors strongly caution against the reader disregarding the bias in $\mathbf{s}'_{(C_k)_k}$ and proceeding along with the least-squares solution from Eq. (46) [or weighted least squares from Eq. (48)] for the sake of “simplicity.” Experiments performed by the authors found that, when integrated with a sequential navigation filter (e.g., extended Kalman filter, unscented Kalman filter), the interplay of the bias in $\mathbf{s}'_{(C_k)_k}$ with the navigation states causes significant structure in the state residuals that is not captured by the filter’s formal covariance. This can be severe in some cases. Thus, it is necessary to use an unbiased means of computing the direction of motion $\mathbf{s}'_{(C_k)_k}$.

B. Unbiased Maximum Likelihood Estimation

Computing an unbiased estimate of the direction-of-motion measurement $\mathbf{s}'_{(C_k)_k}$ is essential. An unbiased maximum likelihood estimate (MLE) may be obtained by minimizing the weighted landmark *geometric distance* in each image (instead of the algebraic distance used in the linear least-squares solution), subject to the epipolar constraint. Here, the epipolar constraint is most conveniently written as Eq. (45). Therefore, the cost function becomes

$$J(\xi) = \frac{1}{2} \sum_{i=1}^n (\tilde{\xi}^{(i)} - \xi^{(i)})^T \mathbf{R}_\xi^\dagger (\tilde{\xi}^{(i)} - \xi^{(i)}) \quad (49)$$

subject to $\mathbf{H}\mathbf{s}'_{(C_k)_k} = \mathbf{0}_{n \times 1}$

where \dagger is the pseudoinverse operator and

$$\xi^{(i)} = \begin{bmatrix} \bar{\mathbf{u}}_{k-1}^{(i)} \\ \bar{\mathbf{u}}_k^{(i)} \end{bmatrix} \quad (50)$$

$$\mathbf{R}_\xi = \begin{bmatrix} \mathbf{R}_{\bar{\mathbf{u}}_{k-1}} & \mathbf{0}_{3 \times 3} \\ \mathbf{0}_{3 \times 3} & \mathbf{R}_{\bar{\mathbf{u}}_k} \end{bmatrix} \quad (51)$$

Assuming σ_{uv} is the standard deviation of a landmark’s image location (i.e., error in the landmarks apparent $\{u, v\}$ coordinates in units of pixels), the 3×3 covariance matrix $\mathbf{R}_{\bar{\mathbf{u}}_k}$ is

$$\mathbf{R}_{\bar{\mathbf{u}}_{k-1}} = \mathbf{R}_{\bar{\mathbf{u}}_k} = E[\delta \bar{\mathbf{u}}_k^{(i)} \delta \bar{\mathbf{u}}_k^{(i)T}] = \begin{bmatrix} \sigma_{uv}^2 \mathbf{I}_{2 \times 2} & \mathbf{0}_{2 \times 1} \\ \mathbf{0}_{1 \times 2} & 0 \end{bmatrix} \quad (52)$$

It is apparent, therefore, that \mathbf{R}_ξ is a 6×6 matrix of rank 4.

As written, finding the solution to Eq. (49) requires one to explicitly estimate the true image coordinates of each landmark ξ in addition to estimating the direction of motion $\mathbf{s}'_{(C_k)_k}$. This may be done as a straightforward extension of the “gold standard method” [9]. Unfortunately, the parameter vector may become very large if many landmarks are matched. Further, since the number of opportunistic landmark correspondences changes from one image pair to another, the parameter vector to estimate changes dimension from one direction-of-motion measurement to another. Though not necessarily a problem for many terrestrial applications, both the large size and changing dimension of the gold standard method’s parameter vector are undesirable attributes within the context of spacecraft flight software. Fortunately, a nearly equivalent solution may be found without explicit estimation of landmark locations by replacing the geometric distance in Eq. (49) with a first-order approximation (usually called the Sampson distance [9,39]). With this replacement, the parameter vector to estimate becomes just the 3×1 unit vector $\mathbf{s}'_{(C_k)_k}$. Therefore, the cost function of Eq. (49) is now manipulated into a minimization of the weighted Sampson distance. Readers more interested in implementing the solution than the rigorous derivation may skip to the algorithm summary and pseudocode provided in Sec. IV.C.

To find the Sampson distance for this particular problem, begin by writing the i th row of \mathbf{H} from Eq. (42) as

$$\mathbf{h}_i^T = (\bar{\mathbf{u}}_{k-1}^{(i)})^T \mathbf{C}^{-T} \mathbf{M}_{C_{k-1}}^{C_k} [\mathbf{C}^{-1} \bar{\mathbf{u}}_k^{(i)} \times] \quad (53)$$

which are used to adjoin the epipolar constraint for each landmark pair to the cost function via Lagrange multipliers λ_i :

$$\min J'(\xi, \lambda_i) = \frac{1}{2} \sum_{i=1}^n (\tilde{\xi}^{(i)} - \xi^{(i)})^T \mathbf{R}_\xi^\dagger (\tilde{\xi}^{(i)} - \xi^{(i)}) + \sum_{i=1}^n \lambda_i \mathbf{h}_i^T \mathbf{s}'_{(C_k)_k} \quad (54)$$

To find the MLE solution, apply the first differential condition

$$\delta J' = \left[-(\tilde{\xi}^{(i)} - \xi^{(i)})^T \mathbf{R}_\xi^\dagger + \lambda_i (\mathbf{s}'_{(C_k)_k})^T \frac{\partial \mathbf{h}_i}{\partial \xi^{(i)}} \right] \delta \xi^{(i)} = 0 \quad (55)$$

which produces the result

$$\mathbf{R}_\xi^\dagger (\tilde{\xi}^{(i)} - \xi^{(i)}) = \lambda_i \left(\frac{\partial \mathbf{h}_i}{\partial \xi^{(i)}} \right)^T \mathbf{s}'_{(C_k)_k} \quad (56)$$

The partial $\partial \mathbf{h}_i / \partial \xi^{(i)}$ may be computed analytically,

$$\frac{\partial \mathbf{h}_i}{\partial \xi^{(i)}} = \begin{bmatrix} \frac{\partial \mathbf{h}_i}{\partial \bar{\mathbf{u}}_{k-1}^{(i)}} & \frac{\partial \mathbf{h}_i}{\partial \bar{\mathbf{u}}_k^{(i)}} \end{bmatrix} \quad (57)$$

where

$$\frac{\partial \mathbf{h}_i}{\partial \bar{\mathbf{u}}_{k-1}^{(i)}} = - \left[\mathbf{C}^{-1} \bar{\mathbf{u}}_k^{(i)} \times \right] \mathbf{M}_{C_k}^{C_{k-1}} \mathbf{C}^{-1} \quad (58)$$

$$\frac{\partial \mathbf{h}_i}{\partial \bar{\mathbf{u}}_k^{(i)}} = \left[\mathbf{M}_{C_k}^{C_{k-1}} \mathbf{C}^{-1} \bar{\mathbf{u}}_{k-1}^{(i)} \times \right] \mathbf{C}^{-1} \quad (59)$$

Continue by left multiplying Eq. (56) by $(\tilde{\xi}^{(i)} - \xi^{(i)})^T$:

$$(\tilde{\xi}^{(i)} - \xi^{(i)})^T \mathbf{R}_{\tilde{\xi}}^\dagger (\tilde{\xi}^{(i)} - \xi^{(i)}) = \lambda_i (\tilde{\xi}^{(i)} - \xi^{(i)})^T \left(\frac{\partial \mathbf{h}_i}{\partial \xi^{(i)}} \right)^T \mathbf{s}'_{(C_k)_k} \quad (60)$$

The Sampson distance is a first-order approximation of the geometric distance. Thus, take the Taylor series expansion of $\tilde{\mathbf{h}}$ and retain only first-order terms

$$\tilde{\mathbf{h}}_i = \mathbf{h}_i + \frac{\partial \mathbf{h}_i}{\partial \xi^{(i)}} (\tilde{\xi}^{(i)} - \xi^{(i)}) + \dots \quad (61)$$

such that

$$(\tilde{\mathbf{h}}_i - \mathbf{h}_i)^T \approx (\tilde{\xi}^{(i)} - \xi^{(i)})^T \left(\frac{\partial \mathbf{h}_i}{\partial \xi^{(i)}} \right) \quad (62)$$

Recalling the constraint $\mathbf{h}_i^T \mathbf{s}'_{(C_k)_k} = 0$, substitute Eq. (62) into the right-hand side of Eq. (60) to yield the important intermediate result

$$(\tilde{\xi}^{(i)} - \xi^{(i)})^T \mathbf{R}_{\tilde{\xi}}^\dagger (\tilde{\xi}^{(i)} - \xi^{(i)}) \approx \lambda_i \tilde{\mathbf{h}}_i^T \mathbf{s}'_{(C_k)_k} \quad (63)$$

To find a solution for λ_i , return to Eq. (56) and right multiply by $\mathbf{R}_{\tilde{\xi}}^{1/2}$:

$$\mathbf{R}_{\tilde{\xi}}^{\dagger/2} (\tilde{\xi}^{(i)} - \xi^{(i)}) = \lambda_i \mathbf{R}_{\tilde{\xi}}^{1/2} \left(\frac{\partial \mathbf{h}_i}{\partial \xi^{(i)}} \right)^T \mathbf{s}'_{(C_k)_k} \quad (64)$$

After taking the inner product of both sides with themselves,

$$(\tilde{\xi}^{(i)} - \xi^{(i)})^T \mathbf{R}_{\tilde{\xi}} (\tilde{\xi}^{(i)} - \xi^{(i)}) = \lambda_i^2 (\mathbf{s}'_{(C_k)_k})^T \left(\frac{\partial \mathbf{h}_i}{\partial \xi^{(i)}} \right)^T \mathbf{R}_{\tilde{\xi}} \left(\frac{\partial \mathbf{h}_i}{\partial \xi^{(i)}} \right)^T \mathbf{s}'_{(C_k)_k} \quad (65)$$

one may solve for λ_i^2

$$\lambda_i^2 = \frac{(\tilde{\xi}^{(i)} - \xi^{(i)})^T \mathbf{R}_{\tilde{\xi}}^\dagger (\tilde{\xi}^{(i)} - \xi^{(i)})}{(\mathbf{s}'_{(C_k)_k})^T \left(\frac{\partial \mathbf{h}_i}{\partial \xi^{(i)}} \right) \mathbf{R}_{\tilde{\xi}} \left(\frac{\partial \mathbf{h}_i}{\partial \xi^{(i)}} \right)^T \mathbf{s}'_{(C_k)_k}} \quad (66)$$

Now, returning to Eq. (63) and squaring both sides,

$$[(\tilde{\xi}^{(i)} - \xi^{(i)})^T \mathbf{R}_{\tilde{\xi}}^\dagger (\tilde{\xi}^{(i)} - \xi^{(i)})]^2 \approx \lambda_i^2 (\mathbf{s}'_{(C_k)_k})^T \tilde{\mathbf{h}}_i \tilde{\mathbf{h}}_i^T \mathbf{s}'_{(C_k)_k} \quad (67)$$

and, after substituting for λ_i^2 from Eq. (66), one arrives at the equation for the weighted Sampson distance

$$\begin{aligned} & (\tilde{\xi}^{(i)} - \xi^{(i)})^T \mathbf{R}_{\tilde{\xi}}^\dagger (\tilde{\xi}^{(i)} - \xi^{(i)}) \\ & \approx \frac{(\mathbf{s}'_{(C_k)_k})^T \tilde{\mathbf{h}}_i \tilde{\mathbf{h}}_i^T \mathbf{s}'_{(C_k)_k}}{(\mathbf{s}'_{(C_k)_k})^T \left(\frac{\partial \mathbf{h}_i}{\partial \xi^{(i)}} \right) \mathbf{R}_{\tilde{\xi}} \left(\frac{\partial \mathbf{h}_i}{\partial \xi^{(i)}} \right)^T \mathbf{s}'_{(C_k)_k}} = \frac{d_{S_i}^2}{\sigma_{uv}^2} \end{aligned} \quad (68)$$

where d_{S_i} is the Sampson distance. Observe that the left-hand side is the square of the weighted geometric distance as it appears in the original cost function [see Eq. (49)], which has been rewritten on

the right-hand side as the square of the weighted Sampson distance. Note that the weighted Sampson distance is an explicit function of $\mathbf{s}'_{(C_k)_k}$ with the epipolar constraint included. The Sampson distance is discussed further in Appendix B.

To compact notation, let

$$\boldsymbol{\Gamma}_i = \tilde{\mathbf{h}}_i \tilde{\mathbf{h}}_i^T \quad (69)$$

$$\begin{aligned} \boldsymbol{\Xi}_i &= \left(\frac{\partial \mathbf{h}_i}{\partial \xi^{(i)}} \right) \mathbf{R}_{\tilde{\xi}} \left(\frac{\partial \mathbf{h}_i}{\partial \xi^{(i)}} \right)^T \\ &= \left(\frac{\partial \mathbf{h}_i}{\partial \bar{\mathbf{u}}_{k-1}^{(i)}} \right) \mathbf{R}_{\bar{\mathbf{u}}} \left(\frac{\partial \mathbf{h}_i}{\partial \bar{\mathbf{u}}_{k-1}^{(i)}} \right)^T + \left(\frac{\partial \mathbf{h}_i}{\partial \bar{\mathbf{u}}_k^{(i)}} \right) \mathbf{R}_{\bar{\mathbf{u}}} \left(\frac{\partial \mathbf{h}_i}{\partial \bar{\mathbf{u}}_k^{(i)}} \right)^T \end{aligned} \quad (70)$$

where measured pixel coordinates are used to find $\tilde{\mathbf{h}}_i$ from Eq. (53) and the partials from Eqs. (58) and (59). The landmark pixel covariance $\mathbf{R}_{\bar{\mathbf{u}}}$ is from Eq. (52). It is observed that the matrices $\boldsymbol{\Gamma}_i$ and $\boldsymbol{\Xi}_i$ are directly computable from the measurements and are independent of $\mathbf{s}'_{(C_k)_k}$. Therefore, substituting Eq. (68) into Eq. (49), the compact version of the MLE cost function in terms of the weighted Sampson distance is given by

$$\min J(\mathbf{s}'_{(C_k)_k}) = \frac{1}{2} \sum_{i=1}^n \frac{(\mathbf{s}'_{(C_k)_k})^T \boldsymbol{\Gamma}_i \mathbf{s}'_{(C_k)_k}}{(\mathbf{s}'_{(C_k)_k})^T \boldsymbol{\Xi}_i \mathbf{s}'_{(C_k)_k}} \quad (71)$$

A lower bound on the expected errors in $\mathbf{s}'_{(C_k)_k}$ from the solution to Eq. (71) may be found from the Kanatani–Cramér–Rao (KCR) bound [40,41]. The traditional Cramér–Rao bound familiar to the spacecraft navigation analyst [32] may not be directly used here because the measurements $\{\tilde{\mathbf{u}}_{k-1}^{(i)}, \tilde{\mathbf{u}}_k^{(i)}\}_{i=1}^n$ are not a function of the state $\mathbf{s}'_{(C_k)_k}$. Instead, the two are related through the epipolar constraint from Eq. (39). The difference is subtle and is explained well in Ref. [40]. Regardless, the KCR lower bound for the cost function of Eq. (71) is known to be a Fisher information matrix of the form [40,41]

$$\mathcal{F}_{\mathbf{s}'_k} = \sum_{i=1}^n \frac{\boldsymbol{\Gamma}_i}{(\mathbf{s}'_{(C_k)_k})^T \boldsymbol{\Xi}_i \mathbf{s}'_{(C_k)_k}} \quad (72)$$

such that the KCR inequality becomes

$$\mathbf{R}_{\mathbf{s}'_k} = E[(\tilde{\mathbf{s}}'_k - \mathbf{s}')(\tilde{\mathbf{s}}'_k - \mathbf{s}')^T] \geq \mathcal{F}_{\mathbf{s}'_k}^{-1} \quad (73)$$

Assuming that the estimator is efficient (which it is found to be in practice), the lower bound is very nearly achieved:

$$\mathbf{R}_{\mathbf{s}'_k}^{-1} \approx \mathcal{F}_{\mathbf{s}'_k} = \sum_{i=1}^n \frac{\boldsymbol{\Gamma}_i}{(\mathbf{s}'_{(C_k)_k})^T \boldsymbol{\Xi}_i \mathbf{s}'_{(C_k)_k}} \quad (74)$$

There are a variety of techniques for finding the solution to Eq. (71) [37,42,43]. This work uses the so-called *fundamental numerical scheme* developed by Chojnacki et al. [37]. The mathematical procedure is straightforward to implement and has been used in other vision-based spacecraft navigation pipelines [44]. To find the optimal and unbiased estimate of $\mathbf{s}'_{(C_k)_k}$, construct the first differential condition for the cost function in Eq. (71):

$$\begin{aligned} \delta J &= (\mathbf{s}'_{(C_k)_k})^T \\ &\times \left[\sum_{i=1}^n \frac{\boldsymbol{\Gamma}_i}{(\mathbf{s}'_{(C_k)_k})^T \boldsymbol{\Xi}_i \mathbf{s}'_{(C_k)_k}} - \sum_{i=1}^n \frac{(\mathbf{s}'_{(C_k)_k})^T \boldsymbol{\Gamma}_i \mathbf{s}'_{(C_k)_k}}{((\mathbf{s}'_{(C_k)_k})^T \boldsymbol{\Xi}_i \mathbf{s}'_{(C_k)_k})^2} \boldsymbol{\Xi}_i \right] \delta \mathbf{s}'_{(C_k)_k} = 0 \end{aligned} \quad (75)$$

Recognizing the matrix in the middle to be symmetric, let X be

$$\mathbf{X} = \sum_{i=1}^n \frac{\boldsymbol{\Gamma}_i}{\left(\mathbf{s}'_{(C_k)_k}\right)^T \boldsymbol{\Xi} \mathbf{s}'_{(C_k)_k}} - \sum_{i=1}^n \frac{\left(\mathbf{s}'_{(C_k)_k}\right)^T \boldsymbol{\Gamma}_i \mathbf{s}'_{(C_k)_k}}{\left(\left(\mathbf{s}'_{(C_k)_k}\right)^T \boldsymbol{\Xi} \mathbf{s}'_{(C_k)_k}\right)^2} \boldsymbol{\Xi}_i \quad (76)$$

or, noting the relation from Eq. (74),

$$\mathbf{X} = \mathbf{R}_{s'_k}^{-1} - \sum_{i=1}^n \frac{\left(\mathbf{s}'_{(C_k)_k}\right)^T \boldsymbol{\Gamma}_i \mathbf{s}'_{(C_k)_k}}{\left(\left(\mathbf{s}'_{(C_k)_k}\right)^T \boldsymbol{\Xi} \mathbf{s}'_{(C_k)_k}\right)^2} \boldsymbol{\Xi}_i \quad (77)$$

such that the unbiased MLE solution for $\mathbf{s}'_{(C_k)_k}$ is given by

$$\mathbf{X} \mathbf{s}'_{(C_k)_k} = \mathbf{0} \quad (78)$$

Observe here that the first term in \mathbf{X} is what one would have found as the solution to Eq. (48) and that the second term accounts for the systematic bias.

As with all problems of this form, the solution for $\mathbf{s}'_{(C_k)_k}$ in Eq. (78) is found by computing the SVD $\mathbf{X} = \mathbf{U} \mathbf{D} \mathbf{V}^T$ and choosing the column of \mathbf{V} corresponding to the smallest singular value in \mathbf{D} . That is, assuming the diagonal of \mathbf{D} consists of the three singular values $d_1 \geq d_2 \geq d_3$ corresponding to the columns of $\mathbf{V} = [\mathbf{v}_1 \ \mathbf{v}_2 \ \mathbf{v}_3]$, the visual odometry direction-of-motion measurement is

$$\tilde{\mathbf{y}} = \tilde{\mathbf{s}}'_{(C_k)_k} = \frac{\tilde{\mathbf{s}}'_{(C_k)_k}}{\|\tilde{\mathbf{s}}'_{(C_k)_k}\|} = \pm \mathbf{v}_3 \quad (79)$$

As with the regular (and biased) least-squares solution, the sign ambiguity for $\tilde{\mathbf{s}}'_{(C_k)_k} = \pm \mathbf{v}_3$ is removed by choosing the unique sign that places the landmark in front of both cameras. To check if the points are in front of the camera is to check for *cheirality* [9,45], which can be done by analytic triangulation of the 3-D location of any one of the matched landmarks in frame C_k . This is discussed in Appendix A.

Importantly, the computation of \mathbf{X} requires knowledge of $\mathbf{s}'_{(C_k)_k}$. An initial guess may be obtained from the linear least-squares solution [see Eq. (46)] and iterated by successive substitution until convergence. Convergence rarely takes more than one to two iterations.

Finally, in order to process the measurements $\tilde{\mathbf{s}}'_{(C_k)_k}$ in a navigation filter, it is necessary to obtain an expression for the measurement covariance. Care must be taken in computing $\mathbf{R}_{s'_k} \approx \mathcal{F}_{s'_k}^{-1}$ since $\mathcal{F}_{s'_k}$ is generally not full rank. To see this, observe that the noise-free matrix \mathbf{H} from Eq. (42) is an $n \times 3$ matrix of rank 2, meaning that $\sum_i \boldsymbol{\Gamma}_i$ is also rank 2 in the absence of measurement noise. Consequently, when processing noisy measurements, $\mathbf{R}_{s'_k}^{-1}$ will be poorly conditioned and direct computation of the inverse is ill-advised. The solution is to once again employ the SVD and compute the pseudoinverse while ignoring the content in the null space of $\mathbf{R}_{s'_k}^{-1}$ (which exists because $\mathbf{s}'_{(C_k)_k}$ is constrained to be a unit vector). Therefore, compute the SVD of Eq. (74) to find

$$\mathbf{R}_{s'_k}^{-1} = \mathbf{U} \mathbf{D} \mathbf{V}^T \quad (80)$$

Note, of course, that \mathbf{U} , \mathbf{D} , and \mathbf{V} found here are different from the SVD of \mathbf{X} . As before, assuming $d_1 \geq d_2 \geq d_3$, the diagonal matrix \mathbf{D} of singular values is

$$\mathbf{D} = \begin{bmatrix} d_1 & 0 & 0 \\ 0 & d_2 & 0 \\ 0 & 0 & d_3 \end{bmatrix} \quad (81)$$

and finding $\mathbf{R}_{s'_k}$ as the pseudoinverse of $\mathbf{R}_{s'_k}^{-1}$ with $d_3 = 0$,

$$\mathbf{R}_{s'_k} = \mathbf{V} \begin{bmatrix} 1/d_1 & 0 & 0 \\ 0 & 1/d_2 & 0 \\ 0 & 0 & 0 \end{bmatrix} \mathbf{U}^T \quad (82)$$

This produces a rank 2 measurement covariance $\mathbf{R}_{s'_k}$ exactly as expected for a unit vector measurement.

C. Visual Odometry Algorithm Summary and Covariance Validation

The discussion in the previous subsections is provided to give the reader a detailed theoretical understanding of the visual odometry algorithm. This detailed development, however, may make the algorithm look more complicated than it is. Therefore, Algorithm 1 aims to clearly outline how the results developed thus far are deployed to create a visual odometry direction-of-motion measurement.

Algorithm 1: Pseudocode to find visual odometry (VO) measurement and covariance

```

1: procedure  $[\tilde{\mathbf{s}}'_{(C_k)_k}, \mathbf{R}_{s'_k}] = \text{VO}(\mathbf{C}, \mathbf{M}_{C_{k-1}}^{C_k}, \{\tilde{\mathbf{u}}_{k-1}^{(i)}, \tilde{\mathbf{u}}_k^{(i)}\}_{i=1}^n)$  ▷ Eq. (23)
2:   compute  $\mathbf{C}^{-1}$ 
3:   for  $i \leftarrow 1$  to  $n$ , do
4:     compute  $\partial \mathbf{h}_i / \partial \tilde{\mathbf{u}}_{k-1}^{(i)}$  and  $\partial \mathbf{h}_i / \partial \tilde{\mathbf{u}}_k^{(i)}$  ▷ Eqs. (58) and (59)
5:     compute  $\boldsymbol{\Gamma}_i$  ▷ Eq. (69)
6:     compute  $\boldsymbol{\Xi}_i$  ▷ Eq. (70)
7:      $\tilde{\mathbf{H}}^T \tilde{\mathbf{H}} \leftarrow \sum_i \boldsymbol{\Gamma}_i$ 
8:      $[\mathbf{U}_H, \mathbf{D}_H, \mathbf{V}_H] \leftarrow \text{svd}(\tilde{\mathbf{H}}^T \tilde{\mathbf{H}})$ 
9:      ${}^{(0)}\mathbf{s}'_{(C_k)_k} \leftarrow \text{last column of } \mathbf{V}_H$ 
10:     $\Delta s \leftarrow 10 \text{ tol}$ 
11:     $m \leftarrow 1$ 
12:    while  $(\Delta s \geq \text{tol}) \wedge (m < m_{\max})$ , do
13:      compute  $\mathbf{R}_{s'_k}^{-1}$  ▷ Eq. (74)
14:      compute  $\mathbf{X}$  ▷ Eq. (77)
15:       $[\mathbf{U}_X, \mathbf{D}_X, \mathbf{V}_X] \leftarrow \text{svd}(\mathbf{X})$ 
16:       ${}^{(m)}\mathbf{s}'_{(C_k)_k} \leftarrow \text{last column of } \mathbf{V}_X$ 
17:       $\Delta s \leftarrow \| {}^{(m)}\mathbf{s}'_{(C_k)_k} - {}^{(m-1)}\mathbf{s}'_{(C_k)_k} \|$ 
18:       $m +$ 
19:       $\tilde{\mathbf{s}}'_{(C_k)_k} \leftarrow {}^{(m)}\mathbf{s}'_{(C_k)_k}$ 
20:      cheirality test to get sign of  $\tilde{\mathbf{s}}'_{(C_k)_k}$  ▷ Appendix A
21:       $[\mathbf{U}_R, \mathbf{D}_R, \mathbf{V}_R] \leftarrow \text{svd}(\mathbf{R}_{s'_k}^{-1})$ 
22:      compute  $\mathbf{R}_{s'_k}$  ▷ Eq. (82)
23: return  $\tilde{\mathbf{s}}'_{(C_k)_k}, \mathbf{R}_{s'_k}$  ▷ visual odometry measurement and covariance
```

The analytic covariance from Eq. (82) may be validated by a Monte Carlo simulation. As an example, consider a calibrated camera with $d_x = d_y = 3000/\text{pixel}$ that begins at an altitude of 50 km above the lunar surface. Let the camera translate by 500 m (0.5 km) and match a total of 25 common surface features uniformly distributed within the overlapping portions of the image pair. Assuming a direction of motion given by

$$\mathbf{s}'_{(C_k)_k} = \begin{bmatrix} 0.5754 \\ -0.1578 \\ 0.8025 \end{bmatrix}$$

and a landmark localization error of $\sigma_{uv} = 0.1$ pixels [see Eq. (52)], the results are as shown in Fig. 4. Note that $\mathbf{R}_{s'_k}$ is rank 2 since it is the covariance of a unit vector, and thus the errors lie in a plane perpendicular to the direction of motion. A comparison of the analytic covariance from Eq. (82) with the sample covariance computed from the Monte Carlo residuals shows very good agreement.

V. Matching of Opportunistic Lunar Surface Features in Digital Imagery

Construction of the visual odometry direction-of-motion measurement requires robust detection and matching of lunar surface features

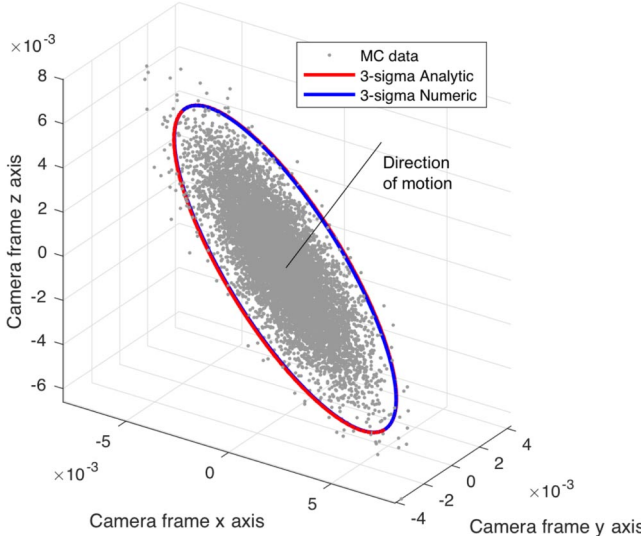


Fig. 4 Comparison of analytic direction-of-motion covariance from Eq. (82) (red ellipse) with results from a 10,000-run Monte Carlo (gray dots) and corresponding covariance (blue ellipse).

in a pair of images. The first task is the detection of salient keypoints that can be well localized in a digital image and that correspond to consistent points on the observed lunar terrain. Then, about each keypoint, the second task is to build a descriptor that may be used to match the same keypoint observed in two (or more) images. There are a great many options available for finding keypoints and building their descriptor, with some of the most popular including the scale-invariant feature transform (known as SIFT) [46], speeded-up robust features (known as SURF) [47], KAZE [48], binary robust invariant scalable keypoints (known as BRISK) [49], and ORB [50]. A comparison of such methods within the context of TRN may be found in Ref. [51]. In addition to these handcrafted features, there has been much recent interest in keypoint detection and feature description using deep learning techniques, such as the learned invariant feature transform (known as LIFT) [52]. Lunar surface features identified in this way (by the automatic detection of keypoints and construction of their corresponding descriptors) are what this work refers to as “opportunistic features/landmarks.” Note that these opportunistic features are in no way related to specific landmarks that a human analyst may intuitively select (e.g., impact craters [53–55]) or the terrain patches used in DEM-based correlation schemes (e.g., Refs. [3,56,57]).

A. Remarks on Feature Repeatability and Lighting Dependence

Despite their differences, all of the feature descriptors considered here (SURF, BRISK, KAZE, and ORB) attempt to encode the unique 2-D intensity pattern surrounding a keypoint in a digital image. It is well established that the appearance of terrain on airless bodies (such as the Moon) is a strong function of the phase angle. Indeed, much of the apparent intensity variation and texture seen in a 2-D digital image

is due to shadows—with changing phase angle (and azimuth) changing the shadows, and hence changing the apparent 2-D intensity patterns within the image. As an example, Fig. 5 shows a comparison of the same terrain patch viewed from a similar vantage point but with very different phase angles. These are real images from the Apollo 17 metric camera (see Sec. VI.B.1 for more on this instrument) and are representative of what to expect in practice. A small counterclockwise rotation occurs going left to right (a consequence of the Apollo command and service module orbit), and two common points are labeled “A” and “B” in each image to assist the reader in comparing the appearance of a particular surface point. It is immediately evident that the local 2-D intensity pattern about potential keypoints is different in each image—thus leading to very different descriptors for the same keypoint under different lighting conditions. Consequently, matching descriptors such as SURF or ORB between two images should only be expected to work when the lighting conditions are nearly the same in both images. Therefore, while feature-based point correspondence works well for sequential images within the context of visual odometry, it is not likely to be an effective means of feature identification when revisiting the same terrain point after many orbits.

Even when considering sequential images, matching of feature descriptors is difficult at low phase angles. This difficulty is due to a variety of effects, with the opposition effect being one of the most challenging. The opposition effect is a surge in reflected brightness around a zero phase angle ($g = 0$) [58] and is known to be especially prominent on the Moon [59,60]. The physical phenomena most responsible for this surge in brightness are 1) shadow hiding of regolith particles near the surface and 2) coherent backscatter. The surge in brightness due to coherent backscatter tends to be fairly narrow ($g < 2$ deg) with the surge due to shadow hiding being considerably wider ($g < 8$ deg). Regardless of the underlying physical cause, tests on real image data (e.g., Sec. VI.B) show a reduced number of landmarks as phase angle decreases—ultimately leading to a degradation in navigation performance. In some cases, this may be mitigated operationally by choosing trajectories or measurement arcs that avoid low phase angles. Improving performance in this regime is a topic of ongoing work.

B. Establishing Feature Correspondence

Suppose that a collection of landmarks are found in a pair of images using a typical feature descriptor (e.g., SURF, KAZE, ORB). Further suppose that correspondence guesses between the features in the image pair are obtained by finding the best descriptor matches (after enforcing a mutual consistency check [13]). In most real image pairs, some of these correspondence guesses will be correct and some of the guesses will be incorrect. The incorrect match assignments must be identified and culled from the set of feature pairs used to compute the direction-of-motion measurement.

This work makes use of a random sample consensus (RANSAC) framework [61] to identify correct and incorrect feature correspondences. Specifically, the algorithm randomly selects a subset of correspondence guesses (at least two matches are required) for each RANSAC trial run. Although the classical RANSAC suggests the minimal set of measurements be used for each trial run, experience

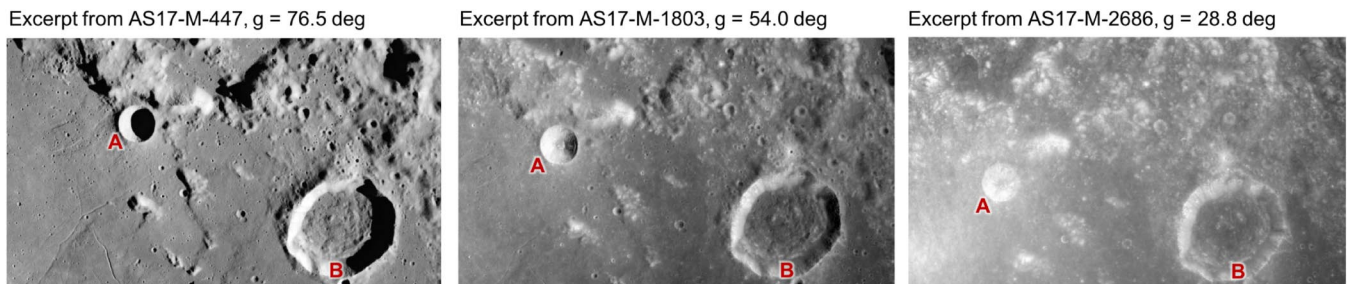


Fig. 5 The appearance of the same terrain changes significantly under different lighting conditions. This example shows three images of the same location collected by the Apollo 17 metric camera in December 1972. (Credit for raw scans of Apollo flight film images: NASA/JSC/ASU.)

with real-world data suggests that using more than the minimal set is desirable when permitted by the system's computational resources [13]. For each RANSAC trial run, the direction of motion is computed using the randomly selected matches. This direction of motion is used to assess geometric consistency of all the matches using the Sampson distance [9,39]

$$d_{S_i}^2 = \frac{[(\bar{\mathbf{u}}_{k-1}^{(i)})^T \mathbf{F}' \bar{\mathbf{u}}_k^{(i)}]^2}{\|\mathbf{SF}' \bar{\mathbf{u}}_k^{(i)}\|^2 + \|\mathbf{SF}'^T \bar{\mathbf{u}}_{k-1}^{(i)}\|^2} \quad (83)$$

where \mathbf{F}' is the nondimensionalized fundamental matrix from Eq. (44), $\bar{\mathbf{u}}_k^{(i)}$ is the homogeneous pixel coordinate of the i th feature in the image from time t_k from Eq. (27), and S is given by

$$\mathbf{S} = [\mathbf{I}_{2 \times 2} \quad \mathbf{0}_{2 \times 1}] \quad (84)$$

Though it is written differently, the Sampson distance from Eq. (83) is equivalent to that from Eq. (68), as discussed in Appendix B. Matches with a Sampson distance of $d_{S_i} \leq d_{S_{\max}}$ (where $d_{S_{\max}}$ is usually around 1–3 pixels) are geometrically consistent with the computed pose (to within $d_{S_{\max}}$) and are considered "inliers." Points with $d_{S_i} > d_{S_{\max}}$ are considered "outliers." After many RANSAC trial runs are completed, the case with the most number of inliers is

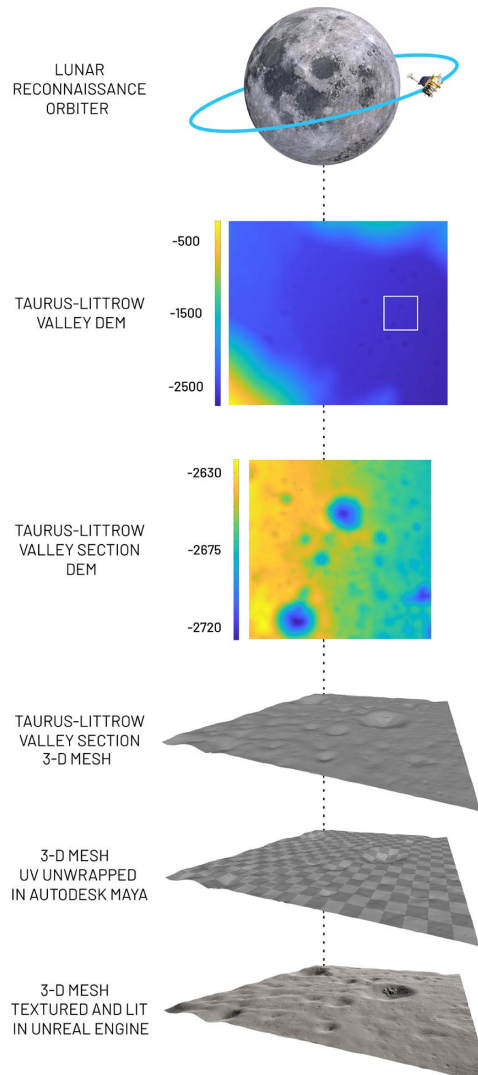


Fig. 6 Overview of the process used to create synthetic images of the Moon's Taurus-Littrow valley using a DEM constructed from LROC data [62].

selected. All of the inliers are considered valid matches and used to compute the final direction of motion measurement.

VI. Validation of Visual Odometry Measurement Generation

A. Validation on Synthetic Imagery: Lunar Reconnaissance Orbiter DEM of the Taurus–Littrow Valley

1. Development of Synthetic Imagery Pipeline

This work evaluates the efficacy of TRN during a lunar descent using synthetic imagery. The simulation environment used to create these synthetic test images is built on a virtual model of the Moon's Taurus–Littrow valley (TLV) developed by Hong et al. in Ref. [62]. The virtual model was developed using the procedure summarized in Fig. 6, which makes use of the digital elevation model of the TLV [63] produced via photogrammetry with images from the Lunar Reconnaissance Orbiter Camera (LROC) narrow angle camera [64].

The full Lunar Reconnaissance Orbiter DEM of the Taurus–Littrow valley covers a 13.9×11.7 km section of the lunar surface. It comprises terrain elevation data points arranged in a 9240×7800 grid (total of 72,072,000 data points) with a distance of 1.5 m between each grid data point. The DEM was converted into a quadrilateral (quad) mesh [65] for use within a real-time rendering engine, resulting in mesh with 72 million facets. To reduce run time, a smaller area of 1.98×1.95 km (consisting of only 1.7 million quad facets) was extracted from the mesh.

The raw 1.7 million facet quad mesh (section of the TLV DEM) was prepared using Autodesk Maya. A UV map was created using a standard UV unwrapping approach to allow for downstream texturing of the 3-D mesh. The final product was exported as an FBX file, which preserved the 3-D mesh, UV map, surface smoothing groups, coordinate frames, and other key parameters into a single file.

Unreal Engine 4 (UE4) was used to develop a lunar surface material for the DEM, add realistic lighting, and simulate the synthetic environment using real-time rendering techniques. Film reference photographs taken by the Apollo astronauts (e.g., Fig. 7) were used to inform the look and feel of the simulated lunar surface material.

A custom physically based rendering (PBR) material was created using UE4's node-based material blueprint editor to simulate the appearance of the lunar surface. This custom material used three

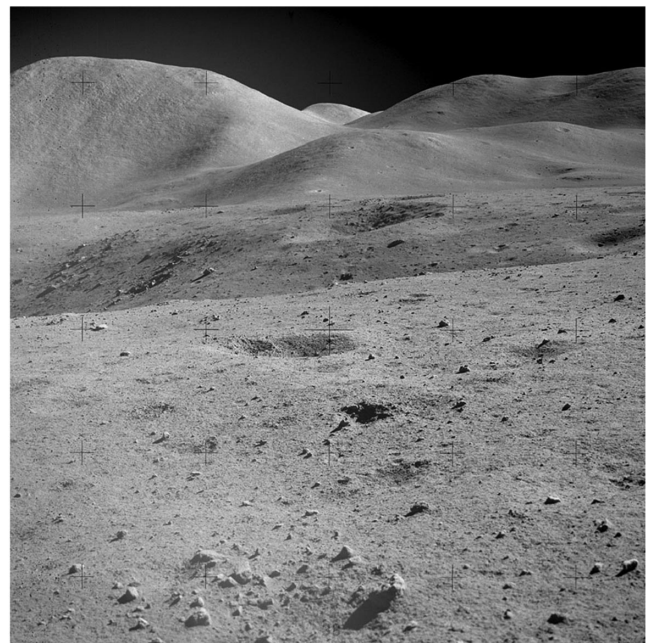


Fig. 7 Example photograph of lunar surface used to inform material properties for the UE4 simulation environment. This photograph (AS15-90-12245) of the lunar Swann Range was collected by Apollo 15 astronaut James B. Irwin on 1 August 1971. Image credit: NASA/Apollo Lunar Surface Journal.

PBR base layers: base color, roughness, and normal. The base color was chosen to resemble that of the lunar regolith. A Fresnel parameter was added onto the base color—UE4 uses Schlick’s approximation for this [66]—to interpolate between 0 and 40% reflection from a layer of dust. The material roughness parameter, which exists on $[0, 1]$, was empirically set to 0.9 to emulate the texture of lunar regolith seen in the Apollo reference photographs.

The new lunar regolith PBR material’s normal layer blends three seamless normal maps of craters, rocks, and pebbles. This gives the illusion of a higher-resolution mesh that would otherwise be too computationally expensive to render. The three normal maps were tiled to make their properties appropriately sized for the DEM, with the craters map tiled by a multiple of five, the rocks at a multiple of 60, and the pebbles at a multiple of 1503. Additionally, a mottled rock alpha mask—tiled by a multiple of 300—was linearly interpolated with the pebbles normal map to allow fine pebbles to show through parts of the alpha mask without completely covering the rock and crater map details.

2. Discussion of TRN Performance

The simulated lunar descent scenario considers a trajectory segment having a flight-path angle of -17.12 deg. A pair of synthetic images were generated for a simulated camera having a 20×30 deg field of view (FOV) and a 1000×1500 pixel focal plane array. This results in the geometry illustrated in Fig. 8.

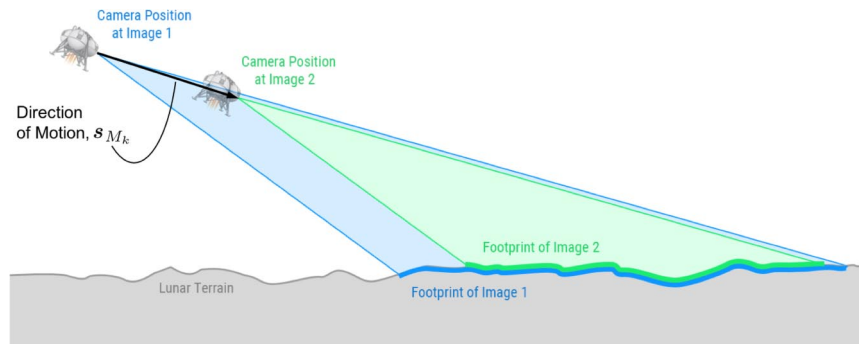


Fig. 8 Illustration of synthetic image configuration (lander not to scale).

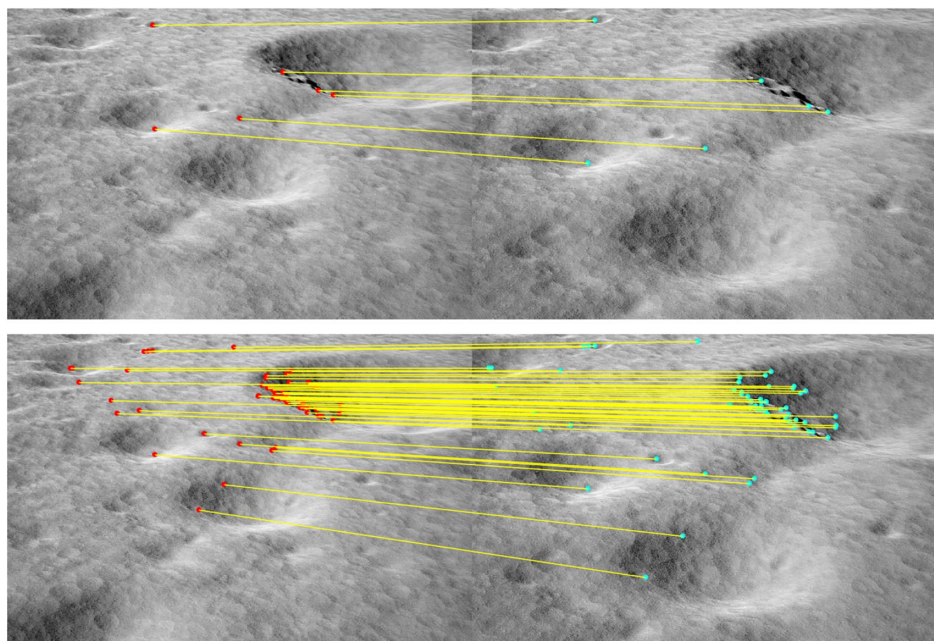


Fig. 9 Example pair of synthetic images during a descent above the Moon’s Taurus–Littrow valley. Feature correspondences are shown for the best six-point RANSAC set (top) and the full set of inliers used to compute the final solution (bottom). This example has 68 inliers.

In this example, SURF features [47] were automatically detected in each digital image and then matched based on their feature descriptors. The RANSAC procedure discussion in Sec. V was employed to find the set of six points producing the most inliers; after which, the entire set of inliers is used to generate the final direction-of-motion solution. The feature correspondences for the best RANSAC solution and for the final set of inliers are shown in Fig. 9.

Applying these methods to this simulated scenario results in the following direction-of-motion results:

$$\tilde{\mathbf{y}} = \frac{\tilde{\mathbf{s}}}{\|\tilde{\mathbf{s}}\|} = \begin{bmatrix} -0.0001 \\ -0.1388 \\ 0.9903 \end{bmatrix} \quad \mathbf{y}_{\text{true}} = \frac{\mathbf{s}}{\|\mathbf{s}\|} = \begin{bmatrix} 0.0000 \\ -0.1575 \\ 0.9875 \end{bmatrix}$$

The angle between the true and estimated directions of motion (which describe the total error in the measurement) is 1.079 deg.

B. Validation on Real Imagery: Apollo 17 Metric Camera

1. The Apollo Metric Camera

This work evaluates the efficacy of TRN in LLO using images of the lunar surface collected by the Apollo 17 metric camera (MC). The Apollo 15, 16, and 17 missions each included a metric camera for the purposes of photogrammetric mapping of the Moon. Located on the service module, the MC was a 114.3×114.3 mm (4.5×4.5 in.)

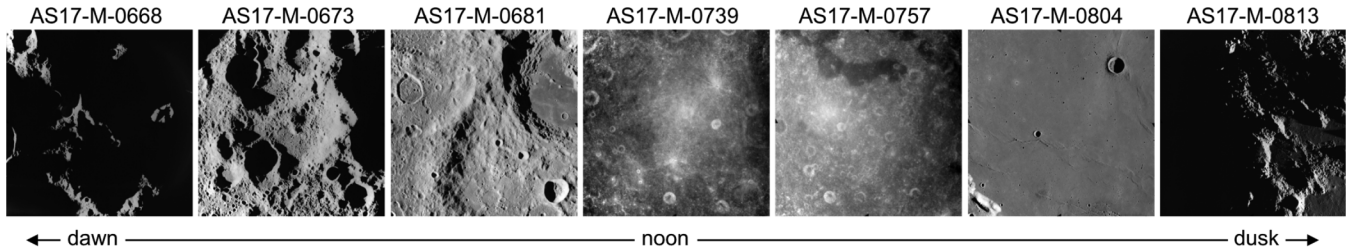


Fig. 10 Sample images of the lunar surface from the Apollo 17 metric camera. (Credit for raw scans of Apollo flight film images: NASA/JSC/ASU.)

format film camera equipped with a lens having an effective focal length of $f = 76.2$ mm (3 in.) [67]. Thus, each square image has a full FOV of about 73.7×73.7 deg. Detailed calibrations of these cameras were preformed for each Apollo mission to support lunar photogrammetry science objectives, with the Apollo 17 MC having a calibrated focal length of $f = 75.842 \pm 0.003$ mm, a principal point offset of $\{x_p, y_p\} = \{-0.005, -0.007\}$ mm, and lens distortions of less than $50 \mu\text{m}$ [68].

The original film images were digitized as part of a joint project between NASA Johnson Space Center (JSC) and Arizona State University (ASU) [69].^{**} Most of the archived images also include metadata related to the position of the camera in both a Moon-centered inertial and MCMF frame (sometimes called the selenocentric and selenographic frames, respectively).

The images are available at varying resolutions, and the present work chose to use the 1012×1012 pixel resolution to best emulate a typical TRN camera. With the resolution of the film digitization known, it is straightforward to compute the camera calibration matrix C from the archived instrument specifications and calibration data. Assuming square pixels, the pixel pitch is computed to be

$$\mu_x = \mu_y = (114.3 \text{ mm})/(1012 \text{ pixel}) = 113 \mu\text{m/pixel}$$

and the values d_x and d_y are then computed directly as

$$\begin{aligned} d_x = d_y &= f/\mu_x = f/\mu_y = (75.842 \text{ mm})/(113 \mu\text{m/pixel}) \\ &= 671.5/\text{pixel} \end{aligned}$$

Likewise the offset of the principal point is about $\{-0.044, -0.062\}$ pixels at the chosen resolution, meaning that $\{u_p, v_p\} = \{506, 506\}$ pixels is a good approximation. Furthermore, the maximum lens distortion is about 0.44 pixels and is ignored in this analysis. Therefore, for a 1012×1012 digitization of the original Apollo 17 metric camera film images, one finds a camera calibration matrix C of

$$C = \begin{bmatrix} d_x & \alpha & u_p \\ 0 & d_y & v_p \\ 0 & 0 & 1 \end{bmatrix} = \begin{bmatrix} 671.5 & 0 & 506 \\ 0 & 671.5 & 506 \\ 0 & 0 & 1 \end{bmatrix} \quad (85)$$

The present analysis considers the complete ensemble of 146 MC images (image numbers AS17-M-0668 to AS17-M-0813) collected during orbit 23 of the Apollo 17 mission (12 December 1972, 16:42:27.021–17:43:19.879 UTC). Each sequential image is separated by about 25 s (image rate of 0.04 Hz). During this portion of the mission, the Apollo command and service module (CSM) had an average altitude about 119 km (ranging from 104.9 to 126.3 km), which corresponds to a 178.5×178.5 km footprint for a perfectly nadir pointed MC image. At the average altitude of 119 km, the digital image ground sample distance (GSD) is about 117 m (at the center of the image) when using a resolution of 1012×1012 pixels. Higher-resolution digitizations available on the archive have a lower GSD.

The image ensemble considered here contains a wide variety of terrain and lighting conditions useful for evaluating the performance

of a TRN system (Fig. 10). The first image is taken just after the Apollo CSM crosses the terminator at a Sun elevation angle near zero (near local dawn). As the spacecraft goes about its orbit on the illuminated side of the Moon, the Sun elevation angle increases to a maximum of about 85 deg (near local noon). The final image is taken just prior to the Apollo CSM crossing over the terminator on its way to the dark side of the Moon (near local dusk). The local terrain casts progressively stronger and more pronounced shadows as the Sun elevation decreases. These shadows play a critical role in establishing good and repeatable landmarks, generally leading to poorer performance at very high Sun elevation angles (see Sec. V.A).

2. Discussion of Feature Correspondence

Sequential image pairs were processed using the techniques described in this paper, with the final product being the camera's direction of motion from the first image to the second. The estimated value is compared to what is expected from the archived metadata. Note that measurement residuals were not computed for a handful of images having either corrupted metadata or no metadata.

After finding features in each image, correspondence guesses are made using feature descriptors and RANSAC is used for robust matching. Each RANSAC trial is performed using only six points, with inliers and outliers being checked based on the Sampson distance. Cases having less than 30 inliers (defined as having a Sampson distance $d \leq \sqrt{5}$ pixel) are rejected. Once the best RANSAC solution is found, the motion of the camera is recomputed using all of the inliers (often many hundreds of points). Examples of the six feature correspondences producing the best RANSAC score are shown for a few example images in Fig. 11. These images were chosen to highlight performance under a variety of lighting conditions and terrain types. Only the six RANSAC points (and not all of the inliers) are shown for clarity. A single example of the best six RANSAC points and all the inliers used to compute the final solution is shown in Fig. 12.

3. Discussion of TRN Performance

The angle between the true and estimated direction of motion (which describes the total error in the measurement) for image pairs in Apollo 17 orbit 23 are shown in Fig. 13. Results are shown for four different feature descriptors: SURF [47], KAZE [48], BRISK [49], and ORB [50]. See Sec. V for additional remarks on these feature descriptors.

When interpreting the performance results in Fig. 13, the reader is cautioned that there is substantial uncertainty in the historical Apollo metadata—hence, it is uncertain how much of the observed direction-of-motion residuals are due to the visual odometry solution. Regardless, residual trends common to all four feature types indicate performance is driven more by image content (or by errors in the historical metadata) than by choice of feature detector. Error trends unique to an individual subplot speak to the relative efficacy of that feature detector. The most noticeable difference between the four subplots occurs between images AS17-M-0738 and AS17-M-0770 (corresponding to low phase angle) where performance is observed to be less reliable.

4. Effect of Phase Angle and Terrain Roughness on Performance

The observed degradation of performance with decreasing phase angle is consistent with the observations of Sec. V.A. To see this more clearly, consider the number of feature descriptors found in each image (more feature descriptors create more opportunity for valid

^{**}Results are archived online at <http://apollo.sese.asu.edu> [retrieved 12 October 2021].

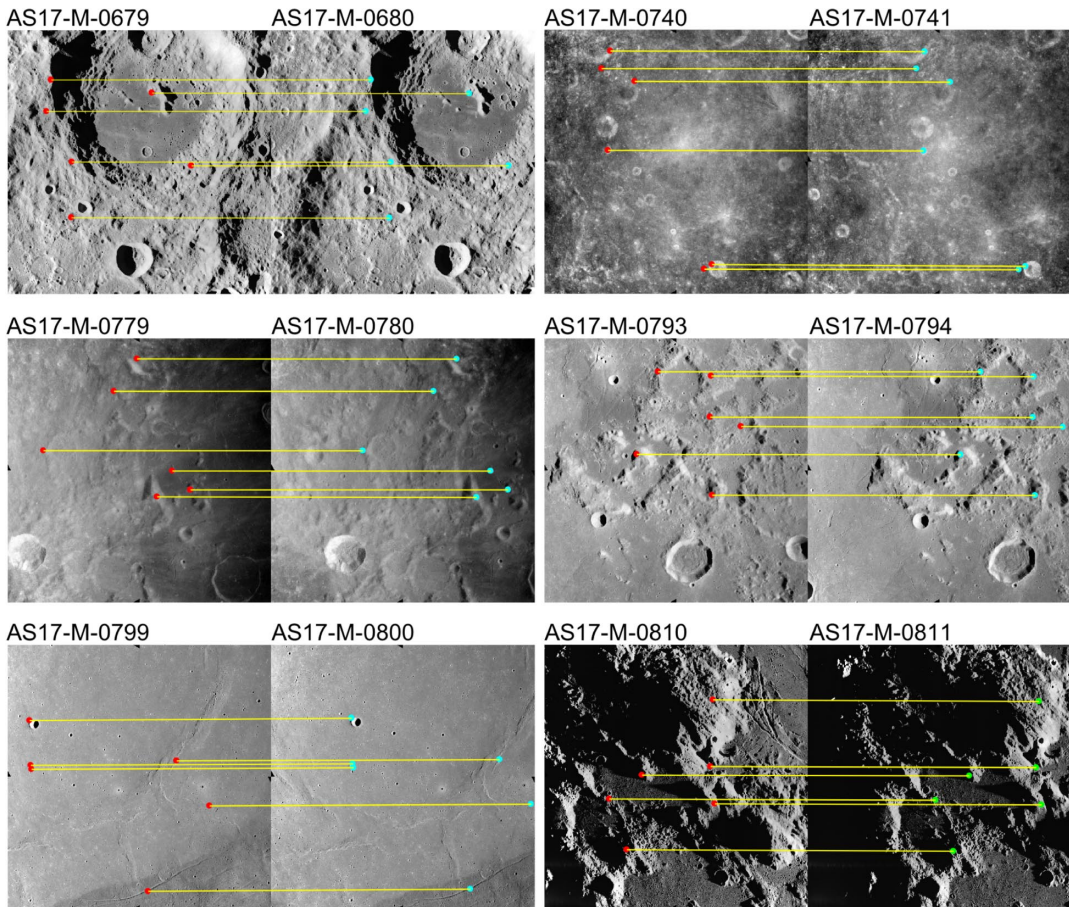


Fig. 11 Example image pairs showing feature correspondences for a wide variety of terrain types and lighting conditions. Only the best six-point RANSAC set is shown. (Credit for raw scans of Apollo flight film images: NASA/JSC/ASU.)

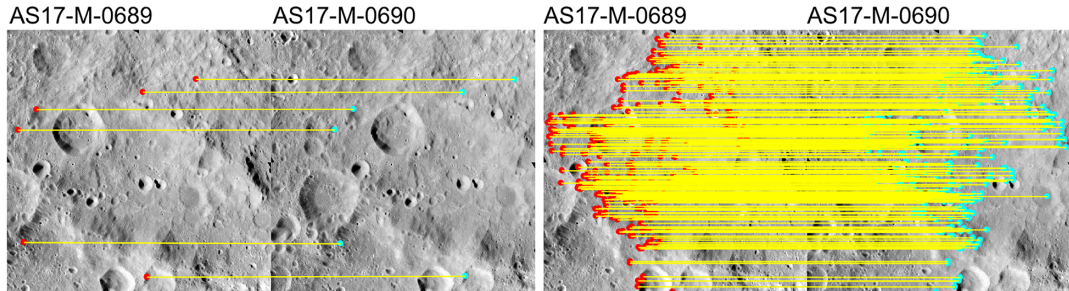


Fig. 12 Example image pair with the best six-point RANSAC set (left) and the full set of inliers used to compute the final solution (right). This example has 288 inliers. (Credit for raw scans of Apollo flight film images: NASA/JSC/ASU.)

matches) concurrently with the phase angle and selenographic longitude—all shown together in Fig. 14.

Looking at images AS17-M-0668 and AS17-M-0708 (before large metadata dropout), the trend of the decreasing number of features with decreasing phase angle is apparent. This trend is observed for all four features considered. Of note, however, is that this trend is not completely reversed as the phase angle increases to comparable levels on the right-hand side (images AS17-M-0771 and AS17-M-0812). This is due to the terrain roughness and the resulting availability of features. The lunar far side is more heavily cratered and mountainous than the lunar near side. Generally, as the phase angle decreases, the rough lunar far-side terrain creates more shadows and texture that generate feature-rich 2-D lighting patterns in images. The near-side terrain, dominated by lunar maria (exemplified by AS17-M-0779 and AS17-M-0800 in Fig. 11), produces comparatively fewer features.

VII. Conclusions

Image-based terrain relative navigation is expected to play a prominent role in future lunar exploration missions. While much work has been devoted to the detection and matching of known surface features (e.g., craters, terrain maplets), this paper investigates the efficacy of image-based TRN with unknown surface features and without any map/catalog of the lunar surface.

The proposed approach—a type of visual odometry—demonstrates that a spacecraft can be navigated by tracking only unknown lunar surface features without ever solving for the 3-D location of those surface features. This is accomplished by producing a visual odometry direction-of-motion measurement through use of the epipolar constraint. A mathematical framework is developed to construct these direction-of-motion measurements from a pair of overlapping digital images and change-in-attitude information from an inertial

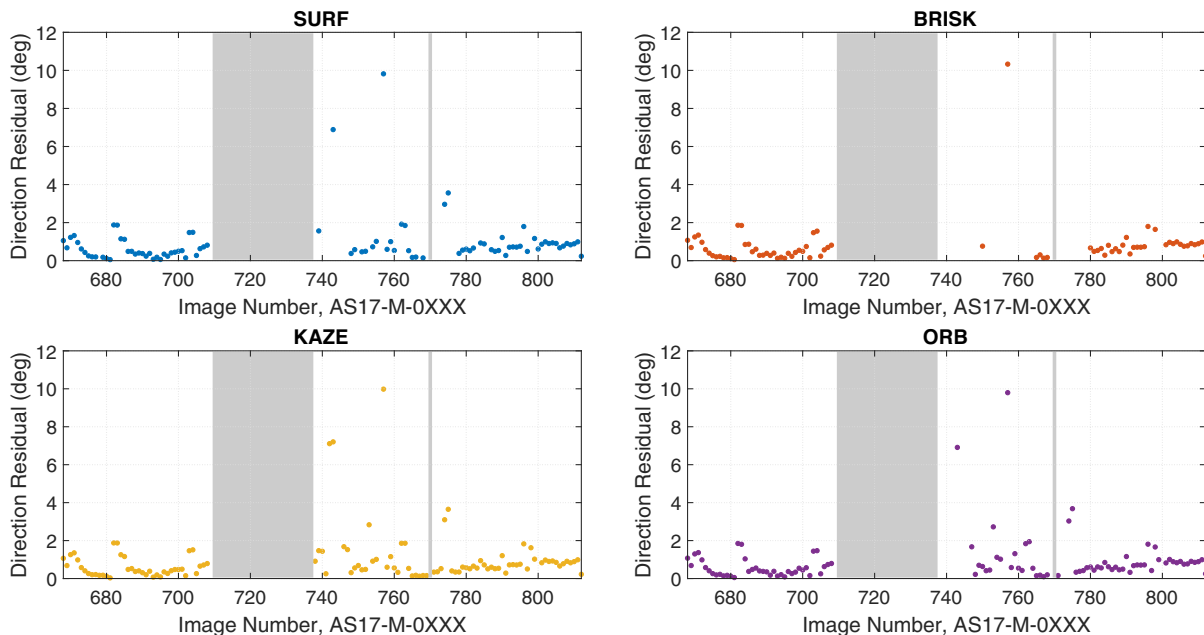


Fig. 13 Error in direction of motion for images on Apollo 17 orbit 23. Gray regions show times where image metadata are missing from the Apollo archive. Substantial uncertainty exists in the historical attitude “truth” data used for comparison.

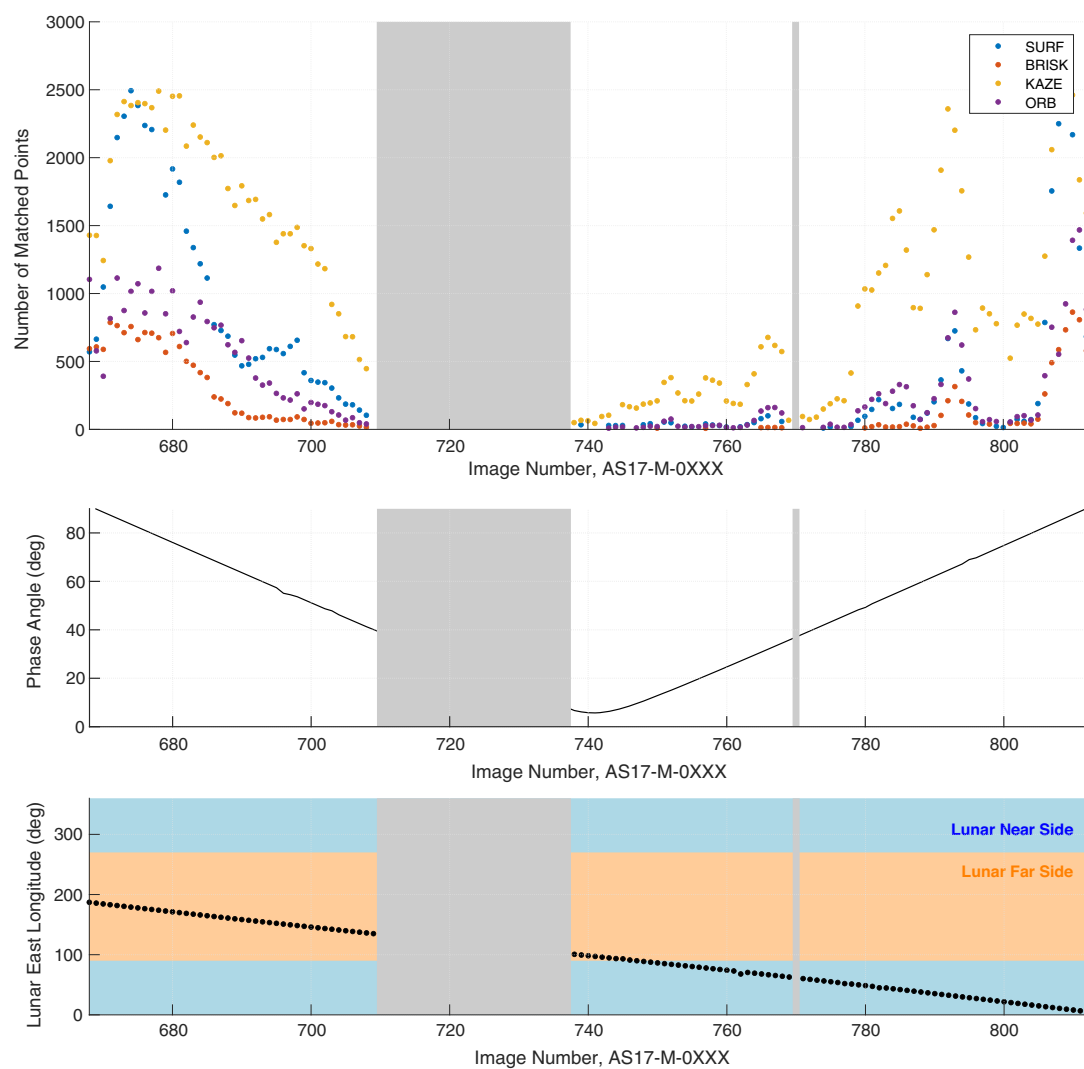


Fig. 14 Number of matched points depends on Sun phase angle for all four feature selectors. Gray regions show times where image metadata are missing from the Apollo archive.

measurement unit. The pixel coordinates of keypoints (i.e., opportunistic landmarks) in each image are detected using well-known methods from computer vision. The correspondences between keypoints in each image are then established using both their feature descriptors and geometric consistency. The reflectance properties of the lunar regolith reduce the efficacy of all common feature descriptors at a low phase angle. This generally results in fewer features to match during times of low phase angle, with fewer features corresponding to degraded navigation performance.

The set of corresponding keypoints (landmarks) from a pair of images is used to construct a maximum likelihood estimate of the spacecraft direction of motion in the camera frame by minimizing the weighted Sampson distance. The authors caution the reader against using a direct least-squares minimization of the algebraic distance, as such a simplification produces a biased measurement. The authors found this bias to cause structured state residuals when integrated with a sequential navigation filter. The measurement formulation summarized in Algorithm 1 does not suffer from such a bias and integrates seamlessly into a typical navigation filter.

The direction-of-motion measurement is demonstrated on synthetic imagery of the Moon's Taurus–Littrow valley and on real imagery from the Apollo 17 metric camera. Both cases demonstrate that the proposed measurement may be produced from images of lunar terrain. It is observed that the reflectance properties of the lunar regolith produce fewer feature correspondences at a low phase angle, resulting in poorer navigation performance under such lighting conditions.

Appendix A: Analytic Landmark Chirality Test by Triangulation

Within the context of multiview geometry and computer vision, a *cheirality test* refers to the process of ensuring that the observed points lie in front of the camera. When computing the direction of motion $\tilde{s}'_{(C_k)_k}$ for the TRN visual odometry solution described in Algorithm 1, the end result is given by Eq. (79) and states that

$$\tilde{s}'_{(C_k)_k} = \pm v_3 \quad (\text{A1})$$

Additional work must be done to resolve this sign ambiguity. One choice of sign places the landmarks in front of both cameras, whereas the other places the landmarks behind the cameras. While there are a variety of ways one may perform this chirality test, a quick solution is available by triangulation of one (or more) landmark.

Consider only the i th landmark. The landmark vectors in each camera frame are given by $\ell'_{(C_{k-1})_{k-1}}^{(i)}$ and $\ell'_{(C_k)_k}^{(i)}$, which may be related to their respective pixel coordinates according to Eqs. (25) and (26):

$$\ell'_{(C_k)_k}^{(i)} = \rho_k^{(i)} \bar{x}_k^{(i)} = \rho_k^{(i)} C^{-1} \bar{u}_k^{(i)} \quad (\text{A2})$$

$$\ell'_{(C_{k-1})_{k-1}}^{(i)} = \rho_{k-1}^{(i)} \bar{x}_{k-1}^{(i)} = \rho_{k-1}^{(i)} C^{-1} \bar{u}_{k-1}^{(i)} \quad (\text{A3})$$

where $\rho_k^{(i)} = \|\ell'_{(C_k)_k}^{(i)}\| / \|\bar{x}_k^{(i)}\|$ and where $\bar{u}_k^{(i)}$ is the homogenous pixel coordinate of landmark i in the image from time t_k , as described in Eq. (27).

The landmark vectors may be normalized by the unknown scale of $s_{(C_k)_k}$, with a “prime” representing the scaled equations. Then, using the geometry from Fig. 2 and the relation from Eq. (11), the MCMF geometry for two sightings of a common landmark is given by the pair of relations

$$\ell'_{(C_k)_k}^{(i)} = \rho_k^{(i)} C^{-1} \bar{u}_k^{(i)} \quad (\text{A4})$$

$$\ell'_{(C_k)_k}^{(i)} = \rho_{k-1}^{(i)} M_{C_k}^{C_{k-1}} C^{-1} \bar{u}_{k-1}^{(i)} - s'_{(C_k)_k} \quad (\text{A5})$$

The difficulty is that the two scalars $\rho_k^{(i)}$ and $\rho_{k-1}^{(i)}$ are unknown. These unknown scalars may be removed from the problem by employing the usual approach for analytic triangulation. Take the cross product of Eq. (A4) with the known vector $C^{-1} \bar{u}_k^{(i)}$,

$$[C^{-1} \bar{u}_k^{(i)} \times] \ell'_{(C_k)_k}^{(i)} = \rho_k^{(i)} [C^{-1} \bar{u}_k^{(i)} \times] C^{-1} \bar{u}_k^{(i)} = \mathbf{0}_{3 \times 1} \quad (\text{A6})$$

and the cross product of Eq. (A5) with the known vector $M_{C_k}^{C_{k-1}} C^{-1} \bar{u}_{k-1}^{(i)}$,

$$\begin{aligned} [M_{C_k}^{C_{k-1}} C^{-1} \bar{u}_{k-1}^{(i)} \times] \ell'_{(C_k)_k}^{(i)} &= \rho_{k-1}^{(i)} [M_{C_k}^{C_{k-1}} C^{-1} \bar{u}_{k-1}^{(i)} \times] M_{C_k}^{C_{k-1}} C^{-1} \bar{u}_{k-1}^{(i)} \\ &\quad - [M_{C_k}^{C_{k-1}} C^{-1} \bar{u}_{k-1}^{(i)} \times] s'_{(C_k)_k} \\ &= -[M_{C_k}^{C_{k-1}} C^{-1} \bar{u}_{k-1}^{(i)} \times] s'_{(C_k)_k} \end{aligned} \quad (\text{A7})$$

These two relations may be stacked into a single linear system

$$\begin{bmatrix} [C^{-1} \bar{u}_k^{(i)} \times] \\ [M_{C_k}^{C_{k-1}} C^{-1} \bar{u}_{k-1}^{(i)} \times] \end{bmatrix} \ell'_{(C_k)_k}^{(i)} = \begin{bmatrix} \mathbf{0}_{3 \times 1} \\ -[M_{C_k}^{C_{k-1}} C^{-1} \bar{u}_{k-1}^{(i)} \times] s'_{(C_k)_k} \end{bmatrix} \quad (\text{A8})$$

which may be solved for $\ell'_{(C_k)_k}^{(i)}$. Note that everything other than $\ell'_{(C_k)_k}^{(i)}$ is known in Eq. (A8). If the z component of $\ell'_{(C_k)_k}^{(i)}$ is greater than zero, then the observed point is in front of the image. It is easy to see from the bottom row of Eq. (A8) that changing the sign of $s'_{(C_k)_k}$ changes the sign $\ell'_{(C_k)_k}^{(i)}$, hence changing the sign of $s'_{(C_k)_k}$ moves the triangulated landmark point to the other side of the camera. This disambiguates the sign of Eq. (79) and Eq. (A1)—one simply chooses the unique sign for $s'_{(C_k)_k}$ that results in the z component of $\ell'_{(C_k)_k}^{(i)}$ being positive.

Finally, while the solution for $\ell'_{(C_k)_k}^{(i)}$ from Eq. (A8) is perfectly adequate for a chirality test, it is not appropriate for precision landmark localization. If best-in-class localization of a landmark's 3-D location is required for navigation or terrain reconstruction, the triangulation algorithm should minimize the residuals of the geometric distance in each image. The classical solution to the image-based triangulation problem was solved exactly by Hartley and Sturm [70] and requires the solution to a degree-six polynomial. There are numerous very good approximations (e.g., Ref. [71]) that may be used if solving for the six roots of Hartley and Sturm's polynomial is undesirable.

Appendix B: Remarks on the Sampson Distance

The Sampson distance is a first-order approximation of the geometric distance between a measured point and a point belonging to an implicitly defined surface. This distance metric was developed by Sampson in 1982 for the problem of conic fitting [39] and has since been used extensively for many applications—including estimation of the fundamental matrix (or, sometimes, the essential matrix) within the context of visual odometry [9,17,43].

The Sampson distance is used in this work in two important places. First is in estimation of the direction of motion $s_{(C_k)_k}$ from corresponding landmark pairs (analogous to estimation of the fundamental/essential matrix), as shown in Eq. (68). Second is the RANSAC evaluation of geometric consistency of candidate matches to determine inliers and outliers, as shown in Eq. (83). The results of Eqs. (68) and (83) are equivalent—but simply written in different forms based on how the Sampson distance is being used. The remarks that follow seek to make this equivalence explicit.

The Sampson distance as derived in Sec. IV results in an expression for the weighted Sampson distance in Eq. (68). The objective here is to make explicit the equivalence between the Sampson distance from Eq. (68) and Eq. (83) written in terms of a measured point correspondence $\{\tilde{u}_{k-1}^{(i)}, \tilde{u}_k^{(i)}\}$:

$$d_{S_i}^2 = \frac{(\tilde{s}'_{(C_k)_k})^T \boldsymbol{\Gamma}_i \tilde{s}'_{(C_k)_k}}{\sigma_{uv}^{-2} (\tilde{s}'_{(C_k)_k})^T \boldsymbol{\Xi}_i \tilde{s}'_{(C_k)_k}} = \frac{[(\tilde{u}_{k-1}^{(i)})^T \mathbf{F}' \tilde{u}_k^{(i)}]^2}{\|\mathbf{S} \mathbf{F}' \tilde{u}_k^{(i)}\|^2 + \|\mathbf{S} \mathbf{F}'^T \tilde{u}_{k-1}^{(i)}\|^2} \quad (\text{B1})$$

where $\boldsymbol{\Gamma}_i$ is from Eq. (69), $\boldsymbol{\Xi}_i$ is from Eq. (70), \mathbf{F} is the fundamental matrix from Eq. (44), and \mathbf{S} is

$$\mathbf{S} = [\mathbf{I}_{2 \times 2} \quad \mathbf{0}_{2 \times 1}] \quad (\text{B2})$$

This equivalence is demonstrated by showing that the numerator and denominator are equivalent.

Therefore, proceed by recognizing from Eq. (53) that $\tilde{\mathbf{h}}_i^T \mathbf{s}'_{(C_k)_k}$ is the epipolar constraint and may be rewritten according to Eq. (44) as

$$\tilde{\mathbf{h}}_i^T \mathbf{s}'_{(C_k)_k} = (\tilde{\mathbf{u}}_{k-1}^{(i)})^T \mathbf{F}' \tilde{\mathbf{u}}_k^{(i)} \quad (\text{B3})$$

Thus, the numerators in Eq. (B1) may be equated directly

$$\begin{aligned} (\mathbf{s}'_{(C_k)_k})^T \Gamma_i \mathbf{s}'_{(C_k)_k} &= (\mathbf{s}'_{(C_k)_k})^T \tilde{\mathbf{h}}_i \tilde{\mathbf{h}}_i^T \mathbf{s}'_{(C_k)_k} = (\tilde{\mathbf{h}}_i^T \mathbf{s}'_{(C_k)_k})^2 \\ &= [(\tilde{\mathbf{u}}_{k-1}^{(i)})^T \mathbf{F}' \tilde{\mathbf{u}}_k^{(i)}]^2 \end{aligned} \quad (\text{B4})$$

To address the denominator, use the definition of \mathbf{F}' from Eq. (44) to rewrite terms containing the partials contributing to Ξ_i [see Eqs. (58) and (59)]:

$$\begin{aligned} \left(\frac{\partial \mathbf{h}_i}{\partial \tilde{\mathbf{u}}_{k-1}^{(i)}} \right)^T \mathbf{s}'_{(C_k)_k} &= \mathbf{C}^{-T} \mathbf{M}_{C_{k-1}}^{C_k} \left[\mathbf{C}^{-1} \tilde{\mathbf{u}}_k^{(i)} \times \right] \mathbf{s}'_{(C_k)_k} \\ &= -\mathbf{C}^{-T} \mathbf{M}_{C_{k-1}}^{C_k} \left[\mathbf{s}'_{(C_k)_k} \times \right] \mathbf{C}^{-1} \tilde{\mathbf{u}}_k^{(i)} = -\mathbf{F}' \tilde{\mathbf{u}}_k^{(i)} \end{aligned} \quad (\text{B5})$$

$$\begin{aligned} \left(\frac{\partial \mathbf{h}_i}{\partial \tilde{\mathbf{u}}_k^{(i)}} \right)^T \mathbf{s}'_{(C_k)_k} &= -\mathbf{C}^{-T} \left[\mathbf{M}_{C_k}^{C_{k-1}} \mathbf{C}^{-1} \tilde{\mathbf{u}}_{k-1}^{(i)} \times \right] \mathbf{s}'_{(C_k)_k} \\ &= \mathbf{C}^{-T} \left[\mathbf{s}'_{(C_k)_k} \times \right] \mathbf{M}_{C_k}^{C_{k-1}} \mathbf{C}^{-1} \tilde{\mathbf{u}}_{k-1}^{(i)} = \mathbf{F}'^T \tilde{\mathbf{u}}_{k-1}^{(i)} \end{aligned} \quad (\text{B6})$$

Substituting these results into the definition of Ξ_i from Eq. (70):

$$\begin{aligned} (\mathbf{s}'_{(C_k)_k})^T \Xi_i \mathbf{s}'_{(C_k)_k} &= (\mathbf{F}' \tilde{\mathbf{u}}_k^{(i)})^T \mathbf{R}_{\tilde{\mathbf{u}}} (\mathbf{F}'^T \tilde{\mathbf{u}}_k^{(i)}) \\ &\quad + (\mathbf{F}'^T \tilde{\mathbf{u}}_{k-1}^{(i)})^T \mathbf{R}_{\tilde{\mathbf{u}}} (\mathbf{F}'^T \tilde{\mathbf{u}}_{k-1}^{(i)}) \end{aligned} \quad (\text{B7})$$

Observe now that $\mathbf{R}_{\tilde{\mathbf{u}}}$ from Eq. (52) may be written as

$$\mathbf{R}_{\tilde{\mathbf{u}}} = \sigma_{uv}^2 \mathbf{S}^T \mathbf{S} = \begin{bmatrix} \sigma_{uv}^2 \mathbf{I}_{2 \times 2} & \mathbf{0}_{2 \times 1} \\ \mathbf{0}_{1 \times 2} & 0 \end{bmatrix} \quad (\text{B8})$$

and

$$\begin{aligned} (\mathbf{s}'_{(C_k)_k})^T \Xi_i \mathbf{s}'_{(C_k)_k} &= \sigma_{uv}^2 (\mathbf{S} \mathbf{F}' \tilde{\mathbf{u}}_k^{(i)})^T (\mathbf{S} \mathbf{F}' \tilde{\mathbf{u}}_k^{(i)}) \\ &\quad + \sigma_{uv}^2 (\mathbf{S} \mathbf{F}'^T \tilde{\mathbf{u}}_{k-1}^{(i)})^T (\mathbf{S} \mathbf{F}'^T \tilde{\mathbf{u}}_{k-1}^{(i)}) \end{aligned} \quad (\text{B9})$$

Thus, it is clear that the two denominators in Eq. (B1) are equivalent

$$\sigma_{uv}^{-2} (\mathbf{s}'_{(C_k)_k})^T \Xi_i \mathbf{s}'_{(C_k)_k} = \|\mathbf{S} \mathbf{F}' \tilde{\mathbf{u}}_k^{(i)}\|^2 + \|\mathbf{S} \mathbf{F}'^T \tilde{\mathbf{u}}_{k-1}^{(i)}\|^2 \quad (\text{B10})$$

Acknowledgment

This work was made possible by funding from the Intuitive Machines Lunar Payload and Data Services Program in support of the IM-1 mission.

References

- [1] Johnson, A., and Montgomery, J., "Overview of Terrain Relative Navigation Approaches for Precise Lunar Landing," *2008 IEEE Aerospace Conference*, Inst. of Electrical and Electronics Engineers, Piscataway, NJ, 2008, pp. 1–10. <https://doi.org/10.1109/AERO.2008.4526302>
- [2] Singh, L., and Lim, S., "On Lunar On-Orbit Vision-Based Navigation: Terrain Mapping, Feature Tracking Driven EKF," *AIAA Guidance, Navigation, and Control Conference*, AIAA Paper 2008-6834, 2008. <https://doi.org/10.2514/6.2008-6834>
- [3] Adams, D., Criss, T., and Shankar, U., "Passive Optical Terrain Relative Navigation Using APLNav," *2008 IEEE Aerospace Conference*, Inst. of Electrical and Electronics Engineers, Piscataway, NJ, 2008, pp. 1–9. <https://doi.org/10.1109/AERO.2008.4526303>
- [4] Johnson, A., Villaume, N., Umsted, C., Kourchians, A., Sternberg, D., Trawny, N., Cheng, Y., Geipel, E., and Montgomery, J., "The Mars 2020 Lander Vision System Field Test," *AAS Guidance, Navigation and Control Conference*, American Astronautical Soc. Paper 20-105, San Diego, CA, 2020.
- [5] Toda, F., and Schlee, F., "Autonomous Orbital Navigation by Optical Tracking of Unknown Landmarks," *Journal of Spacecraft and Rockets*, Vol. 4, No. 12, 1967, pp. 1644–1648. <https://doi.org/10.2514/3.29147>
- [6] Levine, G., "A Method of Orbital Navigation Using Optical Sightings to Unknown Landmarks," *AIAA Journal*, Vol. 4, No. 11, 1966, pp. 1928–1931. <https://doi.org/10.2514/3.3820>
- [7] Bellantoni, J., "Unidentified Landmark Navigation," *AIAA Journal*, Vol. 5, No. 8, 1967, pp. 1478–1483. <https://doi.org/10.2514/3.4222>
- [8] Papert, S., "The Summer Vision Project," Artificial Intelligence Group, Vision Memo 100, Massachusetts Inst. of Technology, Cambridge, MA, July 1966, <http://hdl.handle.net/1721.1/6125> [retrieved 12 October 2021].
- [9] Hartley, R., and Zisserman, A., *Multiple View Geometry*, 2nd ed., Cambridge Univ. Press, Cambridge, England, U.K., 2003, pp. 1–21, 98–100, 279–289.
- [10] Cheng, Y., Goguen, J., Johnson, A., Leger, C., Matthies, L., Martin, M. S., and Wilson, R., "The Mars Exploration Rovers Decent Image Motion Estimation System," *IEEE Intelligent Systems*, Vol. 19, No. 3, 2004, pp. 13–21. <https://doi.org/10.1109/MIS.2004.18>
- [11] Nistér, D., Naroditsky, O., and Bergen, J., "Visual Odometry," *Proceedings of the 2004 IEEE Computer Society Conference on Computer Vision and Pattern Recognition*, IEEE Publ., Piscataway, NJ, 2004. <https://doi.org/10.1109/CVPR.2004.1315094>
- [12] Scaramuzza, D., and Fraundorfer, F., "Visual Odometry Part I: The First 30 Years and Fundamentals," *IEEE Robotics and Automation Magazine*, Vol. 18, No. 4, 2011, pp. 80–92. <https://doi.org/10.1109/MRA.2011.943233>
- [13] Fraundorfer, F., and Scaramuzza, D., "Visual Odometry Part II: Matching, Robustness, Optimization, and Applications," *IEEE Robotics and Automation Magazine*, Vol. 19, No. 2, 2012, pp. 78–90. <https://doi.org/10.1109/MRA.2012.2182810>
- [14] Lucas, B., and Kanade, T., "An Iterative Image Registration Technique with an Application to Stereo Vision," *Proceedings of the 7th International Joint Conference on Artificial Intelligence*, 1981, pp. 674–679.
- [15] Shi, J., and Tomasi, C., "Good Features to Track," *1994 Proceedings of IEEE Conference on Computer Vision and Pattern Recognition*, Inst. of Electrical and Electronics Engineers, Piscataway, NJ, 1994, pp. 593–600. <https://doi.org/10.1109/CVPR.1994.323794>
- [16] Zitová, B., and Flusser, J., "Image Registration Methods: A Survey," *Image and Vision Computing*, Vol. 21, No. 11, 2003, pp. 977–1000. [https://doi.org/10.1016/S0262-8856\(03\)00137-9](https://doi.org/10.1016/S0262-8856(03)00137-9)
- [17] Nistér, D., "An Efficient Solution to the Five-Point Relative Pose Problem," *IEEE Transactions on Pattern Analysis and Machine Intelligence*, Vol. 26, No. 6, 2004, pp. 756–770. <https://doi.org/10.1109/TPAMI.2004.17>
- [18] Acton, C. H., Jr., "Ancillary Data Services of NASA's Navigation and Ancillary Information Facility," *Planetary and Space Sciences*, Vol. 44, No. 1, 1996, pp. 65–70. [https://doi.org/10.1016/0032-0633\(95\)00107-7](https://doi.org/10.1016/0032-0633(95)00107-7)
- [19] Acton, C., Bachman, N., Semenov, B., and Wright, E., "A Look Towards the Future in the Handling of Space Science Mission Geometry," *Planetary and Space Sciences*, Vol. 150, Jan. 2018, pp. 9–12. <https://doi.org/10.1016/j.pss.2017.02.013>
- [20] Christensen, R., Geller, D., and Hansen, M., "Linear Covariance Navigation Analysis for Autonomous Lunar Lander Missions," *AAS Guidance, Navigation, and Control Conference*, American Astronautical Soc. Paper 20-095, San Diego, CA, 2020.
- [21] Christensen, R., Geller, D., and Hansen, M., "Linear Covariance Navigation Analysis of Range and Image Measurement Processing for Autonomous Lunar Lander Missions," *2020 IEEE/ION Position, Location and Navigation Symposium (PLANS)*, Inst. of Electrical and Electronics Engineers, Piscataway, NJ, 2020, pp. 1–10. <https://doi.org/10.1109/PLANS50520.2020.9118302>

- Electronics Engineers, Piscataway, NJ, 2020, pp. 1524–1535.
<https://doi.org/10.1109/PLANS46316.2020.9109838>
- [22] Harbison, R. A., Thomas, P. C., and Nicholson, P. C., “Rotational Modeling of Hyperion,” *Celestial Mechanics and Dynamical Astronomy*, Vol. 110, No. 1, 2011, pp. 1–16.
<https://doi.org/10.1007/s10569-011-9337-3>
- [23] Zanetti, R., “Rotations, Transformations, Left Quaternions, Right Quaternions?” *The Journal of the Astronautical Sciences*, Vol. 66, No. 3, 2019, pp. 361–381.
<https://doi.org/10.1007/s40295-018-00151-2>
- [24] Forsyth, D., and Ponce, J., *Computer Vision: A Modern Approach*, Prentice-Hall, Upper Saddle River, NJ, 2003, pp. 216–219.
- [25] Ma, Y., Soatto, S., Košecká, J., and Sastry, S., *An Invitation to 3-D Vision: From Images to Geometric Models*, Springer, New York, 2010, pp. 110–116, 177–181.
- [26] Zhang, Z., “A Flexible New Technique for Camera Calibration,” *IEEE Transactions on Pattern Analysis and Machine Intelligence*, Vol. 22, No. 11, 2000, pp. 1330–1334.
<https://doi.org/10.1109/34.888718>
- [27] Owen, W., “Methods of Optical Navigation,” *AAS/AIAA Space Flight Mechanics Meeting*, American Astronautical Soc. Paper 11-215, San Diego, CA, 2011.
- [28] Christian, J., Benhacine, L., Hikes, J., and D’Souza, C., “Geometric Calibration of the Orion Optical Navigation Camera Using Star Field Images,” *Journal of the Astronautical Sciences*, Vol. 63, No. 4, 2016, pp. 335–353.
<https://doi.org/10.1007/s40295-016-0091-3>
- [29] Christian, J., “Accurate Planetary Limb Localization for Image-Based Spacecraft Navigation,” *Journal of Spacecraft and Rockets*, Vol. 54, No. 3, 2017, pp. 708–730.
<https://doi.org/10.2514/1.A33692>
- [30] Farrenkopf, R. L., “Analytic Steady-State Accuracy Solutions for Two Common Spacecraft Attitude Estimators,” *Journal of Guidance and Control*, Vol. 1, No. 4, 1978, pp. 282–284.
<https://doi.org/10.2514/3.55779>
- [31] Lefferts, E. J., Markley, F. L., and Shuster, M. D., “Kalman Filtering for Spacecraft Attitude Estimation,” *Journal of Guidance, Control, and Dynamics*, Vol. 5, No. 5, 1982, pp. 417–429.
<https://doi.org/10.2514/3.56190>
- [32] Crassidis, J., and Junkins, J., *Optical Estimation of Dynamic Systems*, CRC Press, Boca Raton, FL, 2004, pp. 81–86, 205–207, 421.
- [33] Markley, F., and Crassidis, J., *Fundamentals of Spacecraft Attitude Determination and Control*, Springer, New York, 2014, pp. 37–48, 71, 76–77, 127–128, 239–246, 257–260, 267.
- [34] Longuet-Higgins, H. C., “A Computer Algorithm for Reconstructing a Scene from Two Projections,” *Nature*, Vol. 293, No. 5828, 1981, pp. 133–135.
<https://doi.org/10.1038/293133a0>
- [35] Christian, J., “Autonomous Initial Orbit Determination with Optical Observations of Unknown Planetary Landmarks,” *Journal of Spacecraft and Rockets*, Vol. 56, No. 1, 2019, pp. 211–220.
<https://doi.org/10.2514/1.A34259>
- [36] Zhang, Z., “Determining the Epipolar Geometry and Its Uncertainty: A Review,” *International Journal of Computer Vision*, Vol. 27, No. 2, 1998, pp. 161–195.
<https://doi.org/10.1023/A:1007941100561>
- [37] Chojnacki, W., Brooks, M. J., van den Hengel, A., and Gawley, D., “On the Fitting of Surfaces to Data with Covariances,” *IEEE Transactions on Pattern Analysis and Machine Intelligence*, Vol. 22, No. 11, 2000, pp. 1294–1303.
<https://doi.org/10.1109/34.888714>
- [38] Kanatani, K., “Statistical Optimization for Geometric Fitting: Theoretical Accuracy Bound and High Order Error Analysis,” *International Journal of Computer Vision*, Vol. 80, No. 2, 2008, pp. 167–188.
<https://doi.org/10.1007/s11263-007-0098-0>
- [39] Sampson, P., “Fitting Conic Sections to ‘Very Scattered’ Data: An Iterative Refinement of the Bookstein Algorithm,” *Computer Graphics and Image Processing*, Vol. 18, No. 1, 1982, pp. 97–108.
[https://doi.org/10.1016/0146-664X\(82\)90101-0](https://doi.org/10.1016/0146-664X(82)90101-0)
- [40] Kanatani, K., “Cramer-Rao Lower Bounds for Curve Fitting,” *Graphical Models and Image Processing*, Vol. 60, No. 2, 1998, pp. 93–99.
<https://doi.org/10.1006/gmip.1998.0466>
- [41] Chernov, N., “Statistical Efficiency of Curve Fitting Algorithms,” *Computational Statistics and Data Analysis*, Vol. 47, No. 4, 2004, pp. 713–728.
<https://doi.org/10.1016/j.csda.2003.11.008>
- [42] Leedan, Y., and Meer, P., “Heteroscedastic Regression in Computer Vision: Problems with Bilinear Constraint,” *International Journal of Computer Vision*, Vol. 37, No. 2, 2000, pp. 127–150.
<https://doi.org/10.1023/A:1008185619375>
- [43] Kanatani, K., and Sugaya, Y., “Unified Computation of Strict Maximum Likelihood for Geometric Fitting,” *Journal of Mathematical Imaging and Vision*, Vol. 38, No. 1, 2010, pp. 1–13.
<https://doi.org/10.1007/s10851-010-0206-6>
- [44] Christian, J. A., “Optical Navigation Using Planet’s Centroid and Apparent Diameter in Image,” *Journal of Spacecraft and Rockets*, Vol. 38, No. 2, 2015, pp. 192–204.
<https://doi.org/10.2514/1.G000872>
- [45] Werner, T., and Pajdla, T., “Cheirality in Epipolar Geometry,” *Proceedings Eighth IEEE International Conference on Computer Vision. ICCV 2001*, Inst. of Electrical and Electronics Engineers, Piscataway, NJ, 2001, pp. 548–553.
<https://doi.org/10.1109/ICCV.2001.937564>
- [46] Lowe, D., “Distinctive Image Features from Scale-Invariant Keypoints,” *International Journal of Computer Vision*, Vol. 60, No. 2, 2004, pp. 91–110.
<https://doi.org/10.1023/B:VISI.0000029664.99615.94>
- [47] Bay, H., Ess, A., Tuytelaars, T., and Van Gool, L., “Speeded-Up Robust Features (SURF),” *Computer Vision and Image Understanding*, Vol. 110, No. 3, 2008, pp. 346–359.
<https://doi.org/10.1016/j.cviu.2007.09.014>
- [48] Alcantarilla, P., Bartoli, A., and Davison, A., “KAZE Features,” *European Conference on Computer Vision*, Vol. 7577, Lecture Notes in Computer Science, edited by A. Fitzgibbon, S. Lazebnik, P. Perona, Y. Sato, and C. Schmid, Springer, Berlin, 2012, pp. 214–227.
https://doi.org/10.1007/978-3-642-33783-3_16
- [49] Leutenegger, S., Chli, M., and Siegwart, R., “BRISK: Binary Robust Invariant Scalable Keypoints,” *IEEE International Conference on Computer Vision (ICCV)*, IEEE Publ., Piscataway, NJ, 2011.
<https://doi.org/10.1109/ICCV.2011.6126542>
- [50] Rublee, E., Rabaud, V., Konolige, K., and Bradski, G., “ORB: An Efficient Alternative to SIFT or SURF,” *IEEE International Conference on Computer Vision (ICCV)*, IEEE Publ., Piscataway, NJ, 2011.
<https://doi.org/10.1109/ICCV.2011.6126544>
- [51] Majji, M., Simon, A., Restrepo, C., and Lovelace, R., “A Comparison of Feature Extraction Methods for Terrain Relative Navigation,” *AIAA SciTech Forum*, AIAA Paper 2020-0601, 2020.
<https://doi.org/10.2514/6.2020-0601>
- [52] Yi, K. M., Trulls, E., and Lepetit, V., “LIFT: Learned Invariant Feature Transform,” European Conference on Computer Vision (ECCV), 2016.
https://doi.org/10.1007/978-3-319-46466-4_28
- [53] Ansar, A., and Cheng, Y., “An Analysis of Spacecraft Localization from Descent Image Data for Pinpoint Landing on Mars and Other cratered Bodies,” *Photogrammetric Engineering and Remote Sensing*, Vol. 71, No. 10, 2005, pp. 1197–1204.
<https://doi.org/10.14358/PERS.71.10.1197>
- [54] Cheng, Y., and Ansar, A., “Landmark Based Position Estimation for Pinpoint Landing on Mars,” *IEEE International Conference on Robotics and Automation*, IEEE Publ., Piscataway, NJ, 2005.
<https://doi.org/10.1109/ROBOT.2005.1570338>
- [55] Hanak, C., Crain, T., and Bishop, R., “Crater Identification Algorithm for the Lost in Low Lunar Orbit Scenario,” *AAS Guidance and Control Conference*, American Astronautical Soc. Paper 10-052, San Diego, CA, 2010.
- [56] Gaskell, R. W., Barnouin-Jha, O. S., Scheeres, D. J., Konopliv, A. S., Mukai, T., Abe, S., Saito, J., Ishiguro, M., Kubota, T., Hashimoto, T., and Kawaguchi, J., “Characterizing and Navigating Small Bodies with Imaging Data,” *Meteoritics and Planetary Science*, Vol. 43, No. 6, 2008, pp. 1049–1061.
<https://doi.org/10.1111/j.1945-5100.2008.tb00692.x>
- [57] Olds, R., May, A., Mario, C., Hamilton, R., Debrunner, C., and Anderson, K., “The Application of Optical Based Feature Tracking to OSIRIS-REx Asteroid Sample Collection,” *AAS Guidance, Navigation, and Control Conference*, American Astronautical Soc. Paper 15-124, San Diego, CA, 2015.
- [58] Hapke, B., *Theory of Reflectance and Emittance Spectroscopy*, 2nd ed., Cambridge Univ. Press, Cambridge, England, U.K., 2012, pp. 221–262.
- [59] Buratti, B., Hillier, J., and Wang, M., “The Lunar Opposition Surge: Observations by Clementine,” *Icarus*, Vol. 124, No. 2, 1996, pp. 490–499.
<https://doi.org/10.1006/icar.1996.0225>
- [60] Hapke, B., Nelson, R., and Smythe, W., “The Opposition Effect of the Moon: Coherent Backscatter and Shadow Hiding,” *Icarus*, Vol. 133, No. 1, 1998, pp. 89–97.
<https://doi.org/10.1006/icar.1998.5907>
- [61] Fischler, M., and Bolles, R., “Random Sample Consensus: A Paradigm for Model Fitting with Applications to Image Analysis and Automated Cartography,” *Communications of the ACM*, Vol. 24, No. 6, 1981,

- pp. 381–395.
<https://doi.org/10.1145/358669.358692>
- [62] Hong, L., Thibeault, R., and Christian, J., “Visualizing Space Data in Virtual Reality,” *2nd RPI Space Imaging Workshop*, IEEE Publ., Piscataway, NJ, 2019.
- [63] Haase, I., Wählisch, M., Gläser, P., Oberst, J., and Robinson, M., “Coordinates and Maps of the Apollo 17 Landing Site,” *Earth and Space Science*, Vol. 6, No. 1, 2019, pp. 59–95.
<https://doi.org/10.1029/2018EA000408>
- [64] Robinson, M., Brylow, S., Tschimmel, M., Humm, D., Lawrence, S. J., Thomas, P. C., Denevi, B. W., Bowman-Cisneros, E., Zerr, J., Ravine, M. A., and Caplinger, M. A., “Lunar Reconnaissance Orbiter Camera (LROC) Instrument Overview,” *Space Science Reviews*, Vol. 150, Nos. 1–4, 2010, pp. 81–124.
<https://doi.org/10.1007/s11214-010-9634-2>
- [65] Thibeault, R., Hong, L., Hollenberg, C., and Christian, J., “Triangles vs. Quadrilaterals: Selecting the Right 3D Model Format for Space Science and Exploration,” *2nd RPI Space Imaging Workshop*, IEEE Publ., Piscataway, NJ, 2019.
- [66] Schlick, C., “An Inexpensive BRDF Model for Physically-Based Rendering,” *Computer Graphics Forum*, Vol. 13, No. 3, 1994, pp. 233–246.
<https://doi.org/10.1111/1467-8659.1330233>
- [67] Edmundson, K. L., Alexandrov, O., Archinal, B. A., Becker, K. J., Kirk, R. L., Moratto, Z. M., Nefian, A. V., Richie, J. O., and Robinson, M. S., “Photogrammetric Processing of Apollo 15 Metric Camera Oblique Images,” *International Archives of the Photogrammetry, Remote Sensing and Spatial Information Sciences*, Vol. XLI-B4, IEEE Publ., Piscataway, NJ, 2016.
<https://doi.org/10.5194/isprs-archives-XLI-B4-375-2016>
- [68] Wu, S., and Moore, H., “Experimental Photogrammetry of Lunar Images,” U.S. Government Printing Office, Geological Survey Professional Paper 1046-D, Washington, D.C., 1980.
<https://doi.org/10.3133/pp1046D>
- [69] Lawrence, S. J., Robinson, M. S., Broxton, M., Stopar, J. D., Close, W., Grunsfeld, J., Ingram, R., Jefferson, L., Locke, S., Mitchell, R., and Scarsella, T., “The Apollo Digital Image Archive: New Research and Data Products,” *Proceedings of the NLSI Lunar Science Conference*, IEEE Publ., Piscataway, NJ, 2008.
- [70] Hartley, R. I., and Sturm, P., “Triangulation,” *Computer Vision and Image Understanding*, Vol. 68, No. 2, 1997, pp. 146–157.
<https://doi.org/10.1006/cviu.1997.0547>
- [71] Lindstrom, P., “Triangulation Made Easy,” *IEEE Computer Society Conference on Computer Vision and Pattern Recognition (CVPR)*, IEEE Publ., Piscataway, NJ, 2010.
<https://doi.org/10.1109/CVPR.2010.5539785>